

The temperature and metallicity distributions of the ICM: insights with TNG-Cluster for *XRISM*-like observations

Dimitris Chatzigiannakis ^{1,2*} Annalisa Pillepich ¹ Aurora Simionescu ^{3,4,5} Nhut Truong ^{6,7} and Dylan Nelson ⁸

¹Max-Planck-Institut für Astronomie, Königstuhl 17, D-69117 Heidelberg, Germany

²Fakultät für Physik und Astronomie, Universität Heidelberg, Im Neuenheimer Feld 226, 69120 Heidelberg, Germany

³SRON Netherlands Institute for Space Research, Niels Bohrweg 4, 2300 RA Leiden, The Netherlands

⁴Leiden Observatory, Leiden University, Niels Bohrweg 2, 2300 RA Leiden, The Netherlands

⁵Kavli Institute for the Physics and Mathematics of the Universe (WPI), The University of Tokyo, Kashiwa, Chiba 277-8583, Japan

⁶Center for Space Sciences and Technology, University of Maryland, Baltimore County, 1000 Hilltop Circle, Baltimore, MD 21250, USA

⁷NASA Goddard Space Flight Center, Code 662, Greenbelt, MD 20771, USA

⁸Universität Heidelberg, Zentrum für Astronomie, ITA, Albert-Ueberle-Str. 2, 69120 Heidelberg, Germany

ABSTRACT

The new era of high-resolution X-ray spectroscopy will significantly improve our understanding of the intra-cluster medium (ICM) by providing precise constraints on its underlying physical properties. However, spectral fitting requires reasonable assumptions on the thermal and chemical distributions of the gas. We use the output of TNG-Cluster, the newest addition to the IllustrisTNG suite of cosmological magnetohydrodynamical simulations, to provide theoretical expectations for the multi-phase nature of the ICM across hundreds of $z = 0$ clusters ($M_{500c} = 10^{14.0-15.3} M_{\odot}$) based upon a realistic model for galaxy formation and evolution. We create and analyse, in an observer-like manner, end-to-end *XRISM*/Resolve mock observations towards cluster centres. We then systematically compare the intrinsic properties of the simulated gas with the inferred ones from spectral fitting via a variety of commonly used spectral-emission models. Our analysis suggests that models with a distribution of temperatures, such as `bvlognorm` and `bvgadem`, better describe the complex thermal structure of the ICM, as predicted by TNG-Cluster, but incur biases of 0.5 – 2 keV (16th–84th percentiles). The 1T `bvapec` is too simplistic for the predicted broad temperature distributions, while a 2T double `bvapec` model systematically fails to capture the input temperature structure. However, all spectral emission models systematically underestimate the Fe abundance of the central ICM by ~ 0.1 solar (~ 20 per cent) primarily due to projection effects. Selecting only strong cool core clusters leads to minor improvements on inference quality, removing the majority of outliers but maintaining similar overall biases and cluster-to-cluster scatter.

Key words: X-ray: galaxies: clusters – Galaxies: clusters – Galaxies: clusters: intracluster medium – methods: numerical

1 INTRODUCTION

Galaxy clusters are excellent probes of the large-scale structure of the Universe due to their rarity, masses and preferential position at the knots of the cosmic web (e.g. Allen et al. 2011). Their extended gaseous atmospheres consisting of X-ray emitting plasma, known as the intra-cluster medium (ICM), play a key role in the evolution of large structures, since processes such as mergers, gas accretion from the cosmic web and feedback all leave signatures in the distribution and properties of this gas.

Various X-ray telescopes (e.g. *XMM-Newton*, *Chandra*, *Suzaku*, SRG/eROSITA) have studied the ICM and its thermal and chemical properties across spatial and mass scales (e.g. Kravtsov & Borgani 2012; Mernier et al. 2018; Walker et al. 2019; Mernier et al. 2023, and references therein). However, the low CCD spectral resolution (~ 120 eV) of the detectors so far limits the scope of X-ray analyses. For example, at CCD resolution, the dynamical state of the gas is

hard to assess, as direct measurements of the gas motions cannot be resolved but for very high speeds; similarly, neighbouring emission lines may get blended, complicating the recovery of e.g. the abundances of various elemental species and the extent of the multi-phase thermal structure of the gas. As a result, many simplifying assumptions, such as coupling individual abundances to Iron (Fe) or assuming single temperature gas, have been routinely made.

In the current and upcoming new era of high-resolution X-ray spectroscopy, from *Hitomi* to missions such as *XRISM*¹ and *newAthena*, these issues can be addressed. For example, as shown for Perseus, *Hitomi*'s spectral resolution of ~ 5 eV revealed a wealth of previously-unresolved spectral lines of different species in the 1.8 – 9 keV band (Hitomi Collaboration et al. 2017). *XRISM* has further promised to break the degeneracies in the thermal structure of the gas by providing robust measurements of the various thermal components in clusters.

* E-mail: chatzigiannakis@mpia.de

¹ <https://www.xrism.jaxa.jp/en/>

However, by overcoming many previous degeneracies, systematic uncertainties become a more prominent source of errors. Assumptions made during the analysis of the X-ray spectra – such as the assumed shape of the temperature and metallicity distributions of the ICM or on the atomic libraries describing the emission lines – as well as unavoidable projection effects – all impact inferences, and may lead to significant biases. This can be problematic, especially for science cases that are sensitive to the exact values of cluster properties, such as their metal budgets (e.g. [Gastaldello et al. 2021](#), and references therein) and the X-ray observable-mass relations used for cosmological inference (e.g. most recently [Ghirardini et al. 2024](#)).

Unfortunately, the physical properties of the ICM are sufficiently complex that these issues cannot be assessed empirically. In this case, numerical simulations are useful tools. With the inclusion of ever more and more realistic physical processes, simulations provide an increasingly detailed view of the ICM (e.g. [Nelson et al. 2024](#), and references therein). For example, in past works, simulations of clusters have quantified biases associated with observations, such as the differences between emission- vs. mass-weighted metallicity profiles or the effects of projection effects (e.g. [Biffi et al. 2018](#); [Veronesi et al. 2024](#)). However, no analysis has yet quantified the impact of specific parametric model choices, of e.g. the ICM temperature distribution, when fitting X-ray spectra.

In this work, we aim to assess the systematic effects associated with the inference of the ICM thermal properties and Fe abundance by using varying and complementary spectral-emission models that are routinely adopted in the field. To do so, we use TNG-Cluster ([Nelson et al. 2024](#)), a recent extension of the IllustrisTNG simulations,² which returns a rich and statistically-large sample of simulated galaxy clusters well suited to study the ICM. Based on the IllustrisTNG model ([Weinberger et al. 2017](#); [Pillepich et al. 2018a](#)) applied to a suite of zoom-in cosmological magneto-hydrodynamical simulations, TNG-Cluster not only creates galaxies at $z = 0$ that are consistent with observations, but also – and of relevance to this work – produces the ICM in clusters with overall characteristics that are consistent with observations ([Nelson et al. 2024](#)).

It is thanks to the combination of numerical resolution and the adopted physical modelling that the output of TNG-Cluster is reasonably, if not quantitatively, realistic. This includes a mix of strong, weak and non cool cores ([Lehle et al. 2024](#), [Lehle et al. 2025 submitted](#)), realistic levels of gas velocity dispersion ([Truong et al. 2024](#)) and kinematics ([Ayromlou et al. 2024](#)), a non-negligible amount of cool gas ([Rohr et al. 2024](#), [Staffehl et al. 2025 submitted](#)), a diversity of radio relics ([Lee et al. 2024](#)), and rich X-ray morphologies similar to observations ([Chadayammuri et al. 2024](#)), including cold fronts, shocks, and cavities ([Truong et al. 2024](#); [Prunier et al. 2024](#)). Additionally, the ICM returned by TNG-Cluster exhibits thermodynamical profiles across the 352 clusters – density, temperature, entropy, and pressure – that are in the ballpark of observational inferences ([Lehle et al. 2024](#)). The distribution of cooling radii, derived from spectral fitting on both TNG-Cluster mocks and real Chandra observations, are quantitatively consistent ([Prunier et al. 2025 submitted](#)). And the metallicity profiles appear compatible with available observational results taken at face value ([Nelson et al. 2024](#)). Overall, the realism of the ICM produced by TNG-Cluster further supports the credibility of the analysis we set out.

With TNG-Cluster, we can hence examine the performance of the most commonly used temperature and metallicity models to fit observed X-ray spectra, as we can retrieve the “true” ICM properties

directly from the simulations. Importantly, we do so across a sample of a few hundred clusters at any given redshift, hence providing robust expectations across the diverse cluster population. To make our analysis timely, we focus on the types of observations currently being taken with *XRISM*, specifically of the central regions of nearby galaxy clusters with the soft X-ray spectrometer Resolve, for which we develop an end-to-end mock and analysis pipeline that we apply to the simulated clusters.

This paper is arranged as follows. In Section 2.1 we present our sample of simulated galaxy clusters from TNG-Cluster. In Section 2.2 we describe our end-to-end mocking procedure, used to create *XRISM*/Resolve like observations of our input clusters, and to analyse them. In Section 3.1 we first examine the intrinsic properties of the ICM, as predicted by TNG-Cluster. We then compare the inferences of various spectral modelling approaches on the temperature distribution and Fe abundance in Sections 3.2 and 3.3, respectively. We discuss the reasons and implications of our findings and expand on various effects in Section 4, and summarize in Section 5.

2 DATA AND METHODS

2.1 The TNG-Cluster simulation suite

TNG-Cluster is a collection of 352 zoom-in magnetohydrodynamical simulations of galaxy clusters drawn from a 1 Gpc parent box, with halo masses of $\log_{10}(M_{200c}/M_{\odot}) = [14.2, 15.3]$ i.e. $\log_{10}(M_{500c}/M_{\odot}) = [14.0, 15.3]$. It complements the volume-limited TNG300 simulation ([Springel et al. 2018](#); [Pillepich et al. 2018b](#); [Nelson et al. 2018](#); [Naiman et al. 2018](#); [Marinacci et al. 2018](#)) with the highest halo masses. In particular, a subset of halos with $\log_{10}M_{200c} = 14.5 - 15.0$ at $z = 0$ have been randomly chosen for re-simulation in TNG-Cluster in order to produce a uniform selection, and hence to compensate for the halo mass drop in TNG300, while simultaneously including all halos with $\log_{10}(M_{200c}) > 15$. For a more detailed description of the halo selection we refer to [Nelson et al. \(2024\)](#). Here we summarize additional salient aspects.

TNG-Cluster was simulated with the AREPO code ([Springel 2010](#)) at a resolution of $1.1 \times 10^7 M_{\odot}$ in gas/stellar target mass, matching that of the TNG300 fiducial run. It is fully based on the IllustrisTNG model ([Weinberger et al. 2017](#); [Pillepich et al. 2018a](#)). This includes a variety of processes that are needed to simulate galaxy formation and evolution, such as stellar formation and evolution, metal enrichment from AGB stars, type Ia and type II supernovae by tracking nine elements (H, He, C, N, O, Ne, Mg, Si, and Fe) in addition to Europium, radiative cooling/heating, seeding and growth of SMBH and both stellar and SMBH (thermal and kinetic) feedback.

Λ CDM cosmological parameters from the Planck observations of the cosmic microwave background ([Planck Collaboration et al. 2016](#)) are assumed in TNG-Cluster and throughout this paper: $\Omega_m = 0.3089$, $\Omega_{\Lambda} = 0.6911$, $\Omega_b = 0.0486$, $H_0 = 67.74 \text{ km s}^{-1} \text{ Mpc}^{-1}$, $\sigma_8 = 0.8159$ and $n_s = 0.9667$, consistent with the other IllustrisTNG runs.

2.2 End-to-end *XRISM*/Resolve-like mocks of simulated ICM

In order to quantify the accuracy of the most commonly used X-ray emission models, we generate mock observations of our simulated clusters. In the following sections, we hence describe our end-to-end pipeline for *XRISM*/Resolve-like X-ray mock spectra using TNG-Cluster halos.

² www.tng-project.org

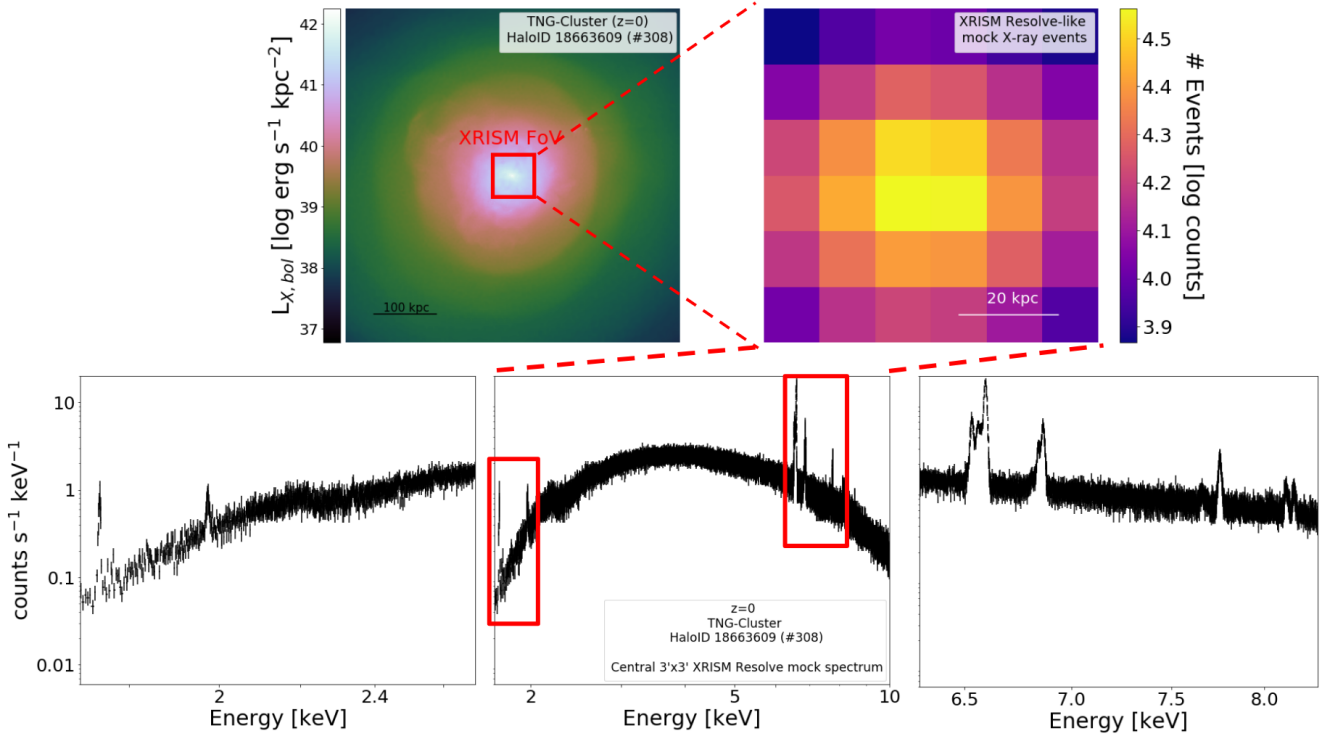


Figure 1. Illustration of the end-to-end *XRISM/Resolve* mocking procedure of simulated clusters from the TNG-Cluster suite. On the top left, we present the intrinsic X-ray luminosity of a randomly-selected cluster from TNG-Cluster, highlighting the FoV of *XRISM/Resolve*, pointing at the centre of the cluster. Following the process described in Section 2.2, we generate a mock event file as if it was observed by *XRISM/Resolve*, presented in the top right corner. The mock spectrum extracted from the event file and a zoom-in on the Fe-K lines are presented in the bottom row. This process showcases our ability in generating high-quality mock spectra from our cosmologically-simulated clusters as if they were observed by *XRISM/Resolve*.

2.2.1 Modeling the intrinsic X-ray signal

First, we model the X-ray emission of the ICM based on the thermodynamical and chemical properties of the simulation gas cells, as predicted by TNG-Cluster. For the purposes of this work, we use the 4.4.0 version of the PyXSIM package (ZuHone et al. 2014) in combination to the SOXS package (ZuHone et al. 2023).

Similar to Truong et al. (2024), for every cluster, we consider as emitting sources all the gas cells that are within the Friend-of-Friend halo and that are within a 3D radius of R_{500c} . Throughout, the centre of a cluster from TNG-Cluster is defined as the minimum of the potential. Furthermore, we assume that all gas cells satisfying the following criteria contribute to the X-ray emission of a given targeted cluster: have a temperature higher than 3×10^5 K (≈ 0.03 keV), a negative net cooling rate, and are not star forming.

For each gas cell, we assume an optically-thin plasma in collisional ionisation equilibrium. We therefore model its emitted spectrum with an *apec* model (i.e. equivalently the *vapec* variant among XSPEC’s models) based on the AtomDB atomic library (v3.0.9 Smith et al. 2001; Foster et al. 2012).

The properties of the gas cells predicted within the TNG-Cluster simulation and relevant for this pipeline are: density, temperature, and absolute elemental abundances (w.r.t. Hydrogen). More specifically, for the latter, we use the TNG-Cluster outcome for all nine elements that the simulation tracks and a relative abundance ratio of X/Fe = 1 for the rest (adopting Asplund et al. 2009), assuming that the absolute Fe abundance is a reasonable proxy of the underlying metal enrichment and that solar abundance ratios hold for those elements. Additionally, we account for the 3D position and velocity

of each gas cell also contribute to the properties of the generated X-ray photons. This allows us to account for effects such as thermal broadening and Doppler shift of the emission lines, producing an accurate representation of the X-ray emission from the ICM of our simulated galaxy clusters.

2.2.2 Observational strategy

In order to generate *XRISM/Resolve* mock event files, namely a list of detected photons of a given energy, from the simulated photons, we first project our halos along the z direction of the simulation box, representing a random direction for each cluster, and place them at the redshift of the Perseus Cluster ($z = 0.0178$), as in Truong et al. (2024). Photoelectric absorption is also applied to the simulated photons, approximating with a *wabs* model the galactic absorption in the position of the Perseus cluster in the sky with a column density of $N_H = 1.38 \times 10^{21} \text{cm}^{-2}$ (Kalberla et al. 2005).

Every cluster is observed with one pointing, focusing on the centre, and hence covering an area given by *XRISM* Field of View (FoV): $3' \times 3'$. In order to best approximate realistic observations of our targets, we also apply *XRISM/Resolve*’s instrumental responses to the intrinsic incoming photons. Namely, we use the Cycle 1 response files, as they have been incorporated in SOXS, for a high resolution ($\sim 5\text{eV}$) response matrix file (RMF) and a standard point-source ancillary response file (ARF) with the gate valve closed.

Regarding the background, as no instrumental background file is publicly available, we ignore it. On the other hand, for the foreground/background signals from the sky, we estimate that resolved point sources, the Cosmic X-ray Background (CXB), thermal emis-

sion from the Milky Way (MW) and the Local Hot Bubble (LHB) all provide a statistically-insignificant amount of detected photons and are effectively ignored in our mocks. This is a direct result of the small detector FoV, and its low efficiency in detecting low-energy photons due to the closed gate valve – their contribution is more relevant in the lower energy regime.

As a result of the procedure above, we obtain mock event files of *XRISM/Resolve*-like observations centred at the cores, unless otherwise specified, of the 352 clusters at $z = 0$ from TNG-Cluster, assuming a reasonable exposure time of 100ks for each system.

Finally, we extract spectra from our event files using the `dmcopy` command from the Chandra Interactive Analysis of Observations (CIAO v.4.16) assuming a default spectral extraction, for the entirety of the FoV of the mock observation. A schematic representation of the result of our mock-observation pipeline can be seen in [Figure 1](#).

2.3 Analysis i.e. fits of *XRISM/Resolve*-like spectra

For the purposes of our analysis, we will be using the X-ray spectral-fitting program *XSPEC* ([Arnaud 1996](#)), using the AtomDB atomic database (v3.0.9), consistent with our X-ray mocks.

Throughout this work, we utilize four commonly-used spectral-emission models with different assumptions on the thermal structure of gas. The models in question are:

- `bvapec`, as the baseline model commonly used to describe the gas: this assumes that the observed ICM is described by a single temperature, i.e. it returns a single-point estimate for its temperature;
- `double bvapec`: this consists of two `bvapec` models and is primarily used to describe two distinct phases of gas (hot and cooler) assuming de facto a binomial thermal structure of the ICM;
- `bvgadem`, which assumes a Normal distribution of ICM temperatures around a central peak;
- `bvlognorm`³, which assumes a Log-Normal distribution of ICM temperatures around a central peak.

For the Fe abundance, all adopted models assume that the observed ICM is described by a single value, as is the case for temperature with the `bvapec` and `double bvapec` models.

We note that for all cases, both the line broadening due to the kinematics of the gas and the abundances of Si, S, Ar, Ca and Ni are also taken into consideration, are modelled independently, and are simultaneously fit for – however, further analysis and their exploitation are beyond the scope of this work.

Regarding our spectral fitting strategy, all our extracted spectra are fitted in the [1.8-10] keV range. Even though the target redshift is known, we allow for the fit to initially vary it over a ± 50 per cent range in order to account for possible bulk motions of the gas along our line of sight. We use a guided approach to fit the model parameters gradually. However, it is still possible for the model to produce a non-valid fit. For this reason we introduce convergence criteria.

2.3.1 Acceptance criteria for spectra best fits

We distinguish between cases where the X-ray spectral fitting is successful (“accepted”) or not (“rejected”). The criteria are as follows.

For both the `bvgadem` and `bvlognorm` models, we require that the uncertainties on the central temperature and on the width of the distributions are smaller than the best-fit values themselves, assuming a signal-to-noise ratio of at least 1 as a minimum requirement for

convergence. For both models, we also require that the width of the assumed distribution is smaller than the best-fit central temperature, as otherwise the model would explicitly return negative temperatures to describe the thermal state of the gas. For the `double bvapec` model, we apply this same convergence criteria to each of the two temperature components, in order for the model to be meaningfully different from the single `bvapec` one.

If a best-fit result fails any of the above criteria, the fit is considered rejected; if it fulfils all of them, it is accepted. We assume by construction that the `bvapec` model is always accepted.

3 RESULTS

In the following sections we compare the ability of different spectral-fitting approaches to return the actual properties of the ICM, as predicted by TNG Cluster. We proceed with a multi-tiered approach.

Firstly, we compare the outputs of the spectral-emission models to the mass-weighted temperature and Fe abundance of the gas in the simulation located in a spherical volume centred at the centre of the cluster, with a radius of $1.5'$ (33.5 kpc at the redshift of Perseus, to approximate *XRISM* FoV): we refer to this as gas in the central sphere or in the 3D cluster centres. Our choice is motivated by the fact that, observationally, one would hope that the output of the extracted spectrum represents the local conditions of the de-projected gas in the region of interest – for us, the *XRISM* FoV at the cluster centre.

We also compare the spectral model inferences to the emission-weighted properties of all the gas in the adopted FoV for a central pointing, namely also considering all the foreground and background ICM gas: we refer to this as gas in a central pointing with a *XRISM*-like FoV. Previous studies have shown that the observed ICM abundance profiles can be better reproduced by weighting the properties of gas particles with emission rather than mass ([Biffi et al. 2017, 2018](#)). Therefore, this can be considered a more apt comparison with our observables and a characterization of the “true” ICM state that is by construction closer to what the spectral fitting can return.

For the purposes of this analysis, we use the emission measure (EM) of each gas cell as its weight:

$$EM = \int n_e n_H dV \simeq n_e n_H V \quad (1)$$

where n_e , n_H the electron and hydrogen number densities and V the volume of the gas cell, tracked by the simulation.

3.1 The complexity of the thermal and chemical structure of cluster centres as predicted by TNG-Cluster

We first quantify the properties of the central X-ray emitting gas, in the ICM of our 352 targets from the TNG-Cluster simulation.

Temperature. Starting with the temperature distribution of the gas in the centre of our clusters ([Figure 2](#), top), we find that, according to TNG-Cluster, the majority of the ICM mass is concentrated around a single temperature. The location of the peak exhibits, as expected, a strong correlation with halo mass, with the central ICM of more massive clusters being, on average, hotter. The width of the temperature distributions varies significantly across clusters, even between systems with similar halo masses. A subset of systems, independent of halo mass, appear to have extended tails of gas, extending to sub-keV temperatures. Considering that we are looking at the centrally-located gas, it is very likely that those tails are associated with the cooler inter-stellar (ISM) or circum-galactic (CGM) media of the brightest cluster galaxy (BCG; see also [Rohr et al. 2024](#)). A few

³ <https://github.com/jeremysanders/lognorm>

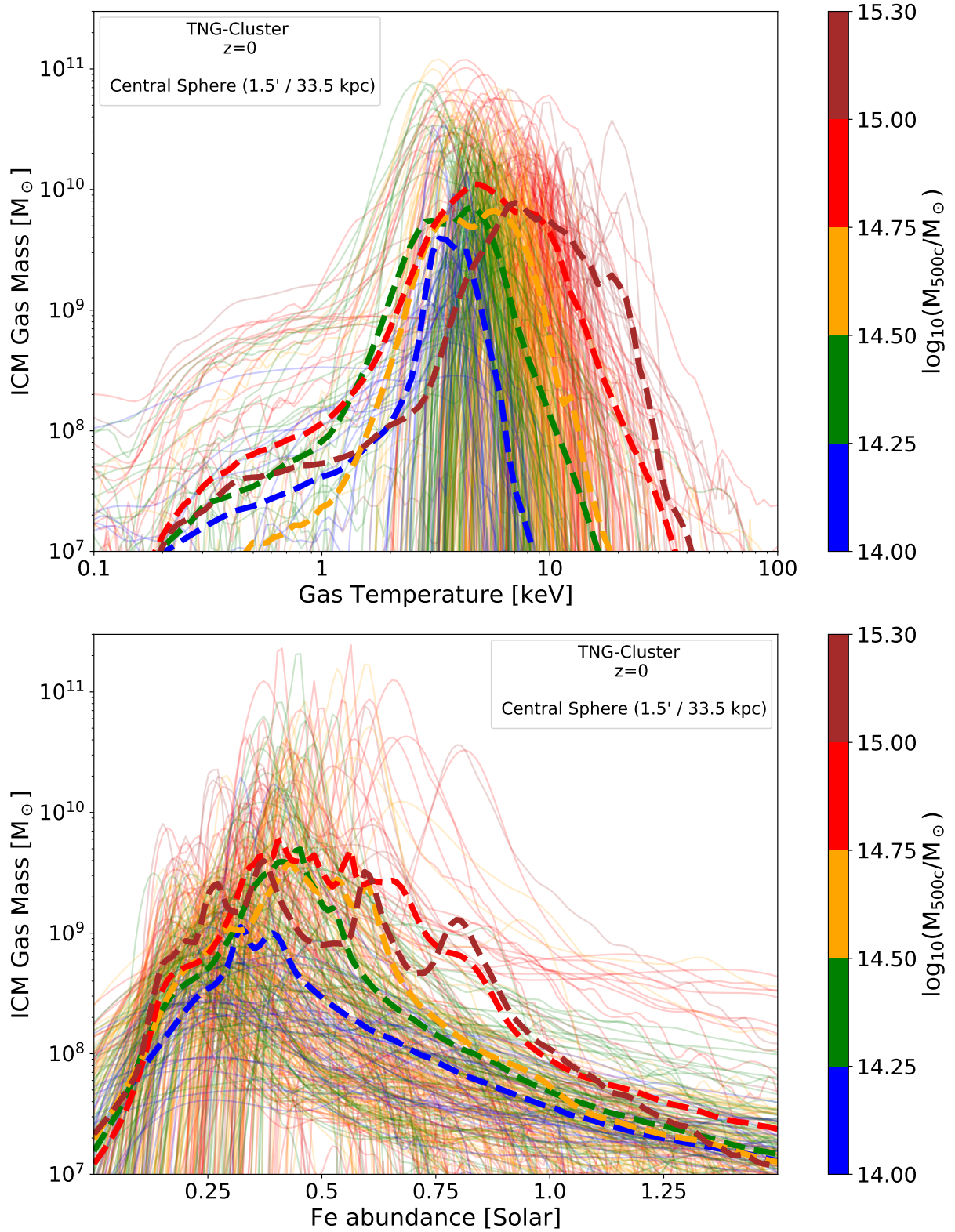


Figure 2. Distributions of the gas temperature (top) and Fe abundance (bottom) for the central ICM of TNG-Cluster halos at $z = 0$. For both cases, each thin solid curve represents the mass-weighted Kernel Density Estimation (KDE) of all the gas cells inside the central 33.5 kpc (1.5' at the redshift of Perseus, to approximate *XRISM* FoV) of a given simulated cluster, colour coded based on the M_{500c} halo mass. The thicker dashed curves indicate the running averages per halo mass bin, as indicated. TNG-Cluster (based on the IllustrisTNG model) predicts extended i.e. broad thermal and Fe abundance distributions for the ICM at the centre of clusters, with a singular peak, but with large variations from cluster to cluster, even for clusters with similar halo masses.

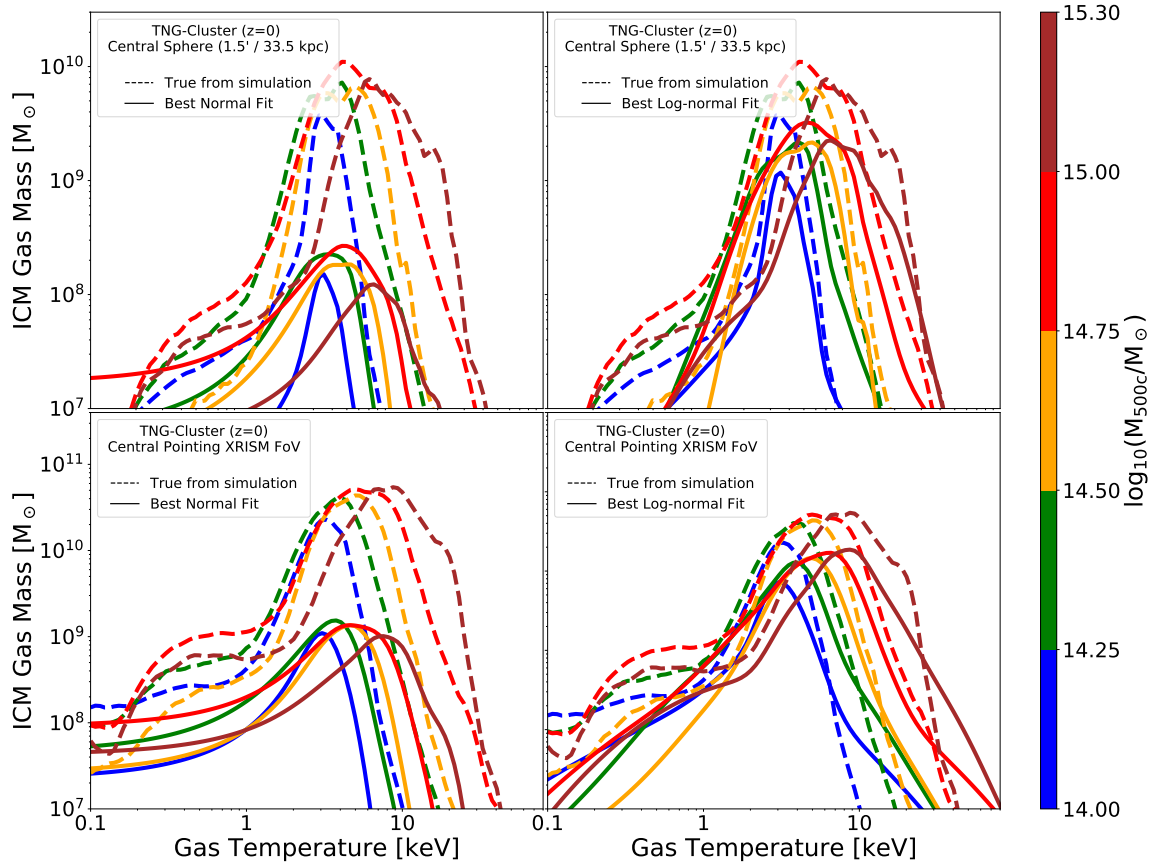


Figure 3. What is the best functional form to describe the temperature distribution of the central ICM of TNG-Cluster? The dashed curves represent the running averages of the mass-weighted gas in the 3D clusters’ centres (top, as in Figure 2) and of the emission-weighted gas for a central pointing with a *XRISM*-like FoV (bottom), binned with respect to M_{500c} halo mass and smoothed via KDE. The solid curves represent the results of fitting the temperature distribution of each simulated cluster with a Normal (left) and Log-Normal (right) functional form, then averaged across all individual clusters in each mass bin. Our analysis indicates that the temperature of the ICM gas at the centre of clusters can be better described by a Log-Normal rather than a Normal distribution, even if the former cannot capture the lower-temperature tails. On the other hand, the Normal distribution misses the peak of the temperature mass in both the mass-weighted and central gas (top) as well as the emission-weighted and FoV gas (bottom).

clusters also exhibit very high, super-virial temperature tails, which, given the SMBH feedback model implemented in TNG-Cluster, may be driven by central energy injections (Truong et al. 2024).

Both the width and shape of the temperature distribution are relevant aspects for our analysis. So, what is the functional form of the temperature of the ICM at the centres of clusters favoured by TNG-Cluster? We fit the temperature distributions with both the Normal and Log-Normal distributions. In Figure 3, we compare the average and best-fit temperature distributions of clusters in halo mass bins, for the intrinsic, mass-weighted gas in the 3D cluster centres (top) and for the emission-weighted gas in a *XRISM*-like FoV (bottom). The corresponding best-fit values of the Log-Normal distribution for each cluster are shown in Figure 4.

We see that the Log-Normal distributions are better descriptors of the temperature. They give a more accurate representation of the overall temperature distribution, even though the cooler sub-keV gas is systematically underestimated. On the other hand, the Normal distribution naturally accounts for the cooler sub-keV gas, but systematically underestimates the width of the underlying distribution towards higher temperatures, especially in more massive halos, and totally misses the peak of the distributions. A drawback of the Log-Normal distribution is that, when considering the emission-weighted temperature of the gas along the line of sight, the log-Normal model

tends to overestimate the hotter tails. Based on Figure 3, the main driver behind this broader width is the enhanced contribution of the sub-keV gas. Because of our weighting scheme, denser gas cells, such as those associated with the ISM or CGM of the BCG, have a stronger contribution on the final distribution and are therefore driving the best-fit width. On the contrary, based on its construction, the Normal best-fit remains fairly unaffected by this enhancement, but it still appears to underestimate the amount of hotter gas present in the emission-weighted temperature distribution.

Overall, our analysis suggests that, while both models are reasonable approximations of the underlying thermal properties of the gas and certainly preferable to single or double temperature models, the Log-Normal functional form is a more accurate representation of the shape of the temperature distribution of the central ICM predicted by TNG-Cluster, consistent with previous works (e.g. Kawahara et al. 2007; Zhuravleva et al. 2013; Khedekar et al. 2013). In Figure 4 we hence provide the best-fit central temperature and standard deviation for the Log-Normal fits, colour coded by the total mass of the cluster. Whereas there is a clear, and known, trend between average central ICM temperature and total cluster mass (spanning between a few keV to more than 10 keV for the studied clusters with $\log_{10}M_{500c} = 14.0 - 15.3$ at $z = 0$), the ICM in each cluster exhibit a diverse range of temperatures, irrespective of total halo mass. Ac-

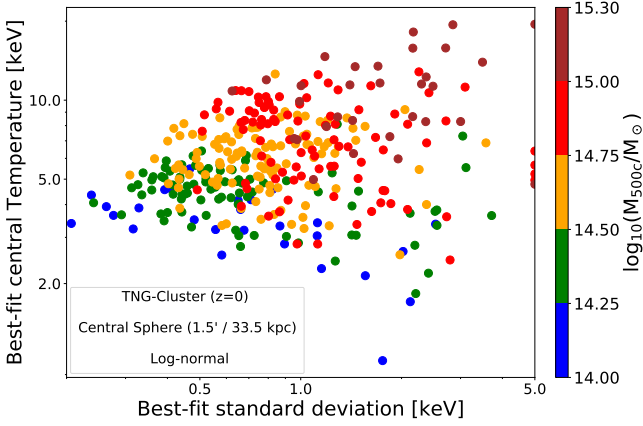


Figure 4. Best-fit parameters of the Log-Normal distribution adopted to describe the ICM temperature of clusters’ centres from TNG-Cluster. We present the central temperature and standard deviation of the best-fit Log-Normal distributions for every TNG-Cluster halo at $z = 0$, colour coded by its M_{500c} halo mass. The average distributions for each mass bin are shown in Figure 2 and Figure 3. While there is an obvious correlation between the best-fit central temperature and the halo mass, no such correlation exists for the standard deviation: how broad the temperature distribution is does not depend on total mass and can vary by an order of magnitude depending on the individual systems.

cording to TNG-Cluster, the Log-Normal width of the central ICM temperature distribution can vary between 0.2 and 10 keV. We note that systems with broader distribution widths have extended sub-keV tails, so it is possible that their best-fit widths are biased high due to the ISM or CGM of the BCG.

Fe abundance. Regarding the Fe abundance of the ICM in the centres of our simulated clusters (Figure 2, bottom), TNG-Cluster predicts large system-to-system variations and broad distributions within individual clusters, across more than one order of magnitude in Solar units.

Upon inspection of all individual systems, the distributions can be broadly described as uni-modal, with the majority of the mass centred around a central peak for the largest majority of the clusters. In fact, we confirm that only a handful of metal-rich clusters exhibit secondary peaks at higher Fe abundances. However, unlike the temperature distributions, the peaks of the Fe abundance distribution show little to no correlation with halo mass: namely, clusters within the same halo mass bins can have significantly different amounts of Fe in their centres. We argue that this is related to their assembly and SMBH feedback histories, and we will expand on this in future works. Indeed, with the TNG model, simulated clusters have been shown to exhibit different central metallicity depending on their cool-core status (Vogelsberger et al. 2018), akin to what suggested by observations. Finally, similar to the tails of cooler gas found in the temperature distributions, a lot of systems tend to have extended tails towards super-solar Fe abundances from gas cells that appear to be associated with the ISM or CGM of the BCG.

Overall, given the broadness of the Fe abundances distributions predicted by TNG-Cluster, the single-metallicity models typically assumed for fitting X-ray spectra are a poor approximation of the metal-enrichment complexity of the centres of clusters.

Model	Accepted fits	Acceptance rate (per cent)
bvapec	352	100
double bvapec	165	47
bvgadem	190	54
bvlognorm	213	61

Table 1. Performance rates of each spectral-emission model adopted to analyse the X-ray spectrum of the central ICM in clusters simulated with TNG-Cluster. We report the number of clusters, among a total of 352 at $z = 0$, for which each model is able to produce an accepted fit for a 100 ks *XRISM/Resolve*-like observation, following the criteria in Section 2.3.1. We also indicate the percentage of valid fits compared to the total, hence indicating their relative acceptance rate. The models that assume unimodal temperature distributions with some width produce accepted fits more often than the double bvapec one.

3.2 Inferring the ICM temperature distribution

As shown and discussed above, as well as in Rohr et al. (2024) and Staffehl et al. 2025 submitted, the intrinsic thermal structure of the ICM, as predicted by TNG-Cluster, is multiphase in nature. Therefore, an important aspect for the accuracy of spectral-emission models is their ability to reflect such a multiphaseness in their best fits – we tackle this next.

Firstly, before quantifying the inference errors, we comment on how frequently it is even possible to successfully fit the X-ray spectra of *XRISM/Resolve*-like observations of the centres of clusters simulated in TNG-Cluster as a function of underlying spectral-modelling choices. Throughout, we adopt the mocking procedure described in Section 2.2 and the fitting analysis and operational definitions of “accepted” and “rejected” fits of Section 2.3.

Based on the success rates reported in Table 1, the bvlognorm model is the best performer, followed by the bvgadem model and the double bvapec, in that order. The bvapec model always provides a valid best fit: however, by assuming a delta function for the temperature distribution, it fails a priori to provide a realistic depiction of the ICM’s thermal properties. For the other models, the success rate can be taken as a measure for the compatibility between the intrinsic and the assumed temperature distributions. Both the bvlognorm and bvgadem models better describe unimodal albeit broad distributions, which is a reasonable approximation for the majority of TNG-Cluster systems. On the other hand, the double bvapec model is performing less well due to a lack of any visible bimodality, i.e. with two similarly-prominent peaks, in the simulated clusters.

Regarding accuracy, we assess first the best-fit values for the primary temperature value (or ICM effective temperature, Figure 5) and then, when appropriate, the width of the distribution (Figure 6). In both cases, we compare the best-fit parameters with the “true” values from the simulations by referring to both the mass-weighted gas properties of the ICM in a central sphere as well as the emission-weighted properties in a central pointing with *XRISM*-like FoV.

ICM effective temperature. For the “true” ICM single-value temperature we take the mean of the temperature distribution from the simulated clusters, i.e. the mean of each input distribution. This is compared against the best-fit values. The mode or median could also be good summary statistics of the TNG-Cluster temperature distributions, but they do not represent the outputs of the bvgadem and bvlognorm models. For the double bvapec model, we consider exclusively the best-fit primary temperature, namely the one that maximizes the relative contribution to the spectrum. We note that for a handful of systems, the double bvapec model finds a hotter, instead of a colder, secondary i.e. subdominant component temperature.

Based on Figure 5, top panels, all models tend to under-predict

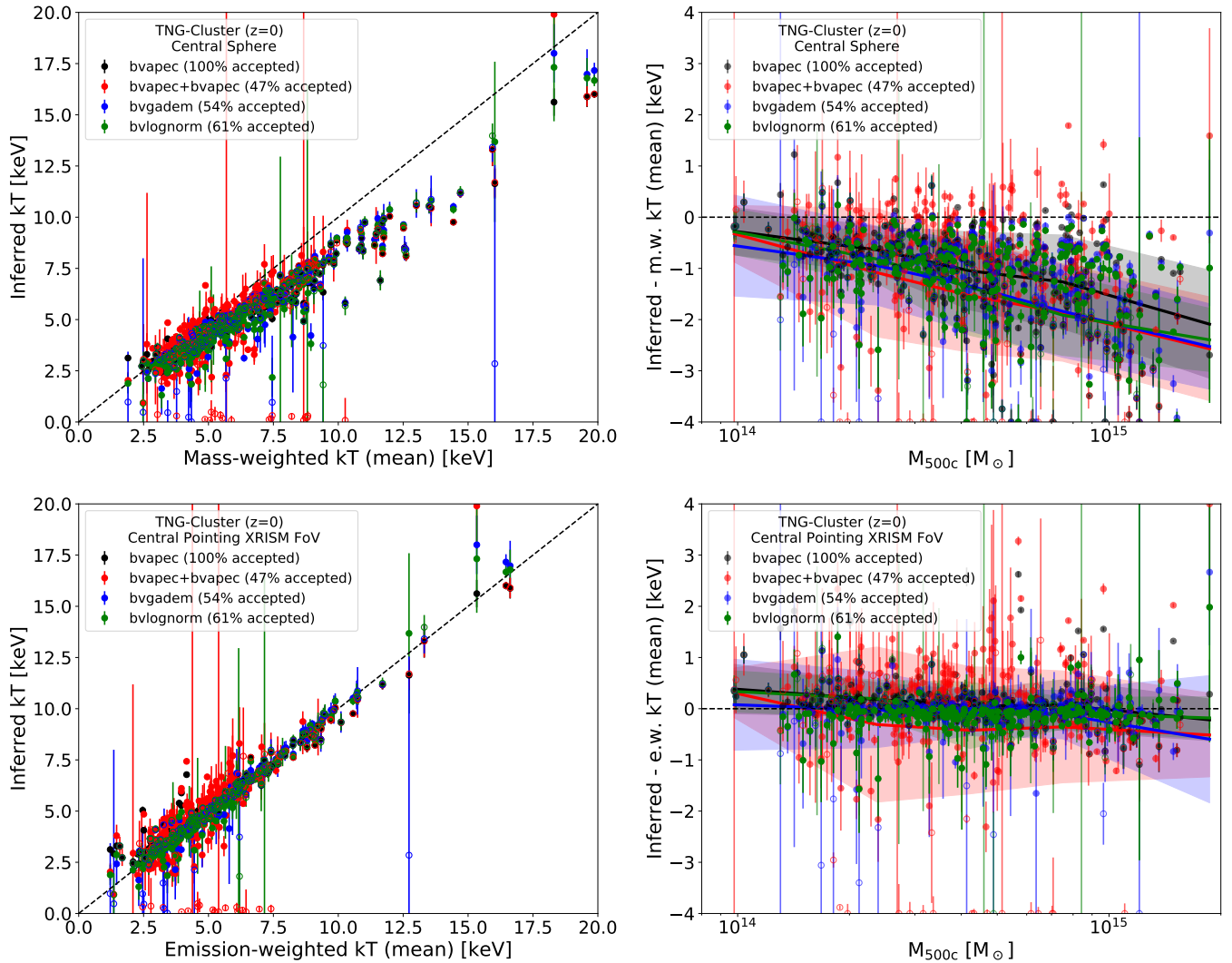


Figure 5. Observational inferences of the ICM temperature at the centre of clusters. In the left panels, we compare the temperature inferred by analysing the X-ray spectra from *XRISM*/Resolve-like observations by adopting a variety of spectral-emission models (different colours) to the true mean temperature of the input temperature distribution, i.e. of systems simulated in TNG-Cluster. In particular, as ground truth, we first consider the mass-weighted gas in the 3D clusters’ centres (top) and then the emission-weighted gas for a central pointing with a *XRISM*-like FoV in a random projection. Filled and empty symbols represent accepted and rejected best fits, respectively (as defined in Section 2.3.1). In the right panels, we indicate the inference offset (or inference error) as a function of each cluster’s M_{500c} halo mass. Solid lines and shaded regions represent the running average and 1σ standard deviation of the difference in bins of $\log_{10}(M_{500c}/M_{\odot})=0.25$. In all panels, the black dashed line represents unity, i.e. perfect accuracy of the model inference. Our results indicate that all models, but to a lesser degree the double bvapec one, are capable of correctly inferring the emission-weighted mean temperature of the gas in the targeted FoV, i.e. accounting for all gas on the line of sight. However, no model returns a best-fit ICM temperature value that is representative of the mass-weighted temperature of the central ICM gas to better than 1 – 2 keV on average.

the mass-weighted mean temperature of the X-ray emitting gas that is actually located in the centre of each cluster. Whereas the bias is systematic, it is in fact relatively small. All models, on average i.e. across the TNG-Cluster sample, underestimate the temperature by 0.8 keV (namely 10 per cent), but with a strong dependence on cluster mass. Namely, the best-fit temperature can underestimate the true one by about 2 keV (20 per cent) at the high-mass end, while being a reasonable approximation for lower-mass clusters. This result underscores the difficulty of assessing the true physical state of central ICM gas. In turn, assuming that TNG-Cluster returns reasonably realistic systems, the top panels of Figure 5 can provide guidelines to correct for this observational-analysis bias. This is the case on

average, whereas for individual clusters the inference error can be much larger – we expand on outlier cases later.

In terms of emission-weighted quantities and comparing to the true properties of all the gas along the line of sight of a *XRISM*-like central pointing (Figure 5, bottom panels), the situation is better, as expected. All models, but to a lesser degree the double bvapec one, produce a best-fit temperature that is indicative of the emission-weighted mean temperature of the gas for a large majority of the studied clusters. The good accuracy of this inference appears independent of halo mass, but the scatter seems to increase somewhat towards the low-mass end. For the double bvapec model, in particular, and for both the top and bottom panels, the inference errors span the largest ranges, with a sizeable fraction of clusters whose

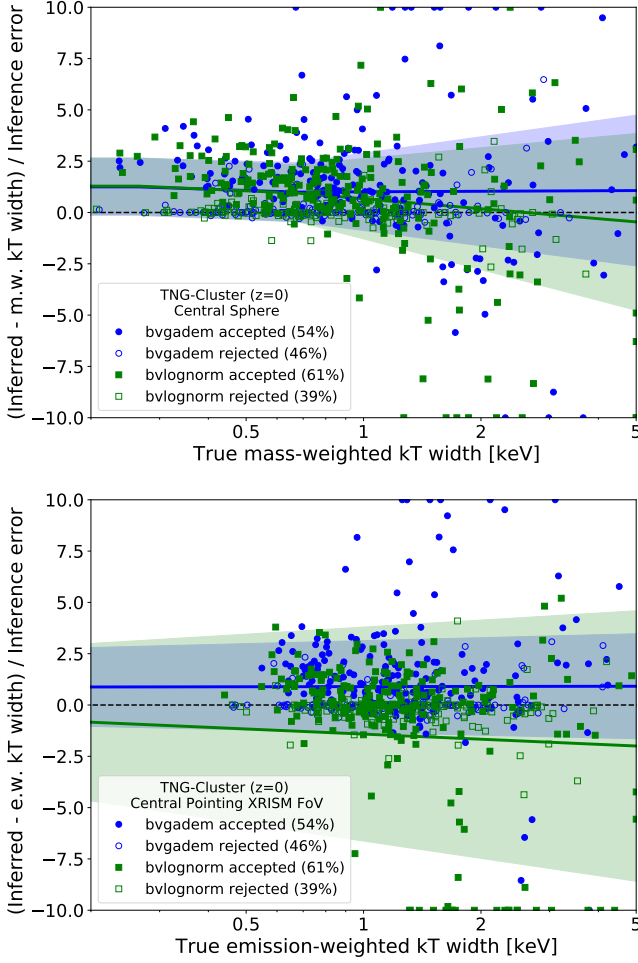


Figure 6. Observational inferences of the width of the temperature distributions of the central ICM. We quantify the residuals of the temperature width for the *bvgadem* and *bvlognorm* models (Equation 2) as a function of the “true” width of the temperature distributions for the mass-weighted central gas (top) or the emission-weighted gas for a central pointing with a *XRISM*-like FoV (bottom), for the same X-ray spectra analysis of Figure 5. Filled and empty symbols show accepted and rejected best fits per-cluster, respectively, while the black dashed line represents unity. Our results suggest that the *bvlognorm* model, compared to *bvgadem*, is on average a more accurate descriptor of the width of the true temperature distributions of the ICM at the centre of clusters (top).

observational-based (primary) temperature is substantially higher or lower than the true one. Moreover, the errors on the best-fit values for the *bvapec* model are on average much larger than in any other case (red error-bars).

We find no significant differences in the quality of the inferences between the accepted and rejected fits, at least according to our definitions. In all cases, they occupy the same parameter space, suggesting that the rejection of the fit does not depend on the inference of the mean mass- or emission-weighted temperature.

ICM temperature width. Beyond the mean temperature, a key parameter in the description of the ICM temperature structure is the width of the distribution. As the “true” value we take the standard deviations of the best-fit Normal and Log-Normal distributions to the intrinsic gas (Figure 3 and Figure 4). We distinguish between the results for the mass-weighted gas in the 3D cluster centre versus emission-weighted gas for a central pointing with a *XRISM*-like

FoV. We then compare these values to the inferred widths from the spectral fitting assuming, respectively, the *bvgadem* and *bvlognorm* spectral-emission models.

In order to assess both the accuracy and the significance of the observational inferences on the underlying thermal properties of the gas, in Figure 6 we show the residuals of the inferred thermal width as a function of the ground truth:

$$\sigma_{\text{res},i} = \frac{\sigma_{\text{inf},i} - \sigma_{\text{true},i}}{\Delta\sigma_{\text{inf},i}}, \quad i = \text{Normal or Log-Normal} \quad (2)$$

where σ_{inf} and $\Delta\sigma_{\text{inf}}$ refer to the distribution width and its 1σ error as inferred by fitting the spectra and where σ_{true} is the true width of the temperature distribution, as predicted by TNG-Cluster. These residuals so defined provide a gauge for the accuracy of the inferred temperature distribution width, at least for the accepted fits; on the other hand, the values in the rejected cases are primarily driven by the denominator and are representative of the higher uncertainties associated with a spectral fit that has not converged.

In Figure 6, we quantify the residuals for both the mass-weighted temperature distribution of the central gas (top) and the emission-weighted gas in a *XRISM*-like FoV (bottom). For both cases, the *bvgadem* model tends to overestimate the width of the distribution, with an average residual of 1.5 (-1.9,+1.7) and 1.5 (-1.6,+1.6), for top and bottom cases, respectively. On the other hand, the *bvlognorm* model has smaller on average residuals for the central mass-weighted gas (0.6 (-1.2,+2.3)) but tends to underestimate the width of the emission-weighted gas in the *XRISM* FoV by an average of -2.1 (-0.01,+3.6). We note that the average value of the *bvlognorm* residuals in the latter case is biased low by a handful of systems for which the model severely underestimates the best-fit width of the emission-weighted temperature distribution.

However, the strong outliers may not arise from the spectral fitting itself, but rather from the inflated value of the best-fit Log-Normal width to the intrinsic gas distribution. As we have shown in Figure 3, the sub-keV gas drives the width of the best-fit Log-Normal distribution towards systematically higher values, due to our weighting scheme, biasing the *bvlognorm* inferences low.

Overall, the *bvlognorm* spectral-emission model can better capture the true width of the broad temperature distribution of the central ICM gas, whether mass-weighted or emission-weighted and including projected contributions.

3.3 Inferring the ICM Fe abundance

We proceed to assess how well observational inferences of the ICM Fe abundance return the “true” underlying values, by following the same procedure as for the temperature, in fact by inspecting the results of the same fits of *XRISM*/Resolve-like spectra from TNG-Cluster discussed thus far.

In Figure 7 we show the comparison between the inferred Fe abundance from all spectral-emission models compared to the mass-weighted mean Fe abundance of the ICM in the actual 3D cluster centre (top) and the emission-weighted mean Fe abundance of gas from a central pointing with a *XRISM*-like FoV (bottom). As the top panel of Figure 7 shows, the inference on the Fe abundance is systematically different of the actual amount of Fe in cluster centres. Namely, all models underestimate the central Fe abundance by 0.11 Solar (21 per cent). The offset varies with halo mass, being larger towards the low- and high-mass end of our mass range. However, the inference error is at least partially driven by the subset of clusters that, despite being actually metal rich, are found to be significantly metal poorer when their X-ray spectra are analysed, irrespective of the adopted

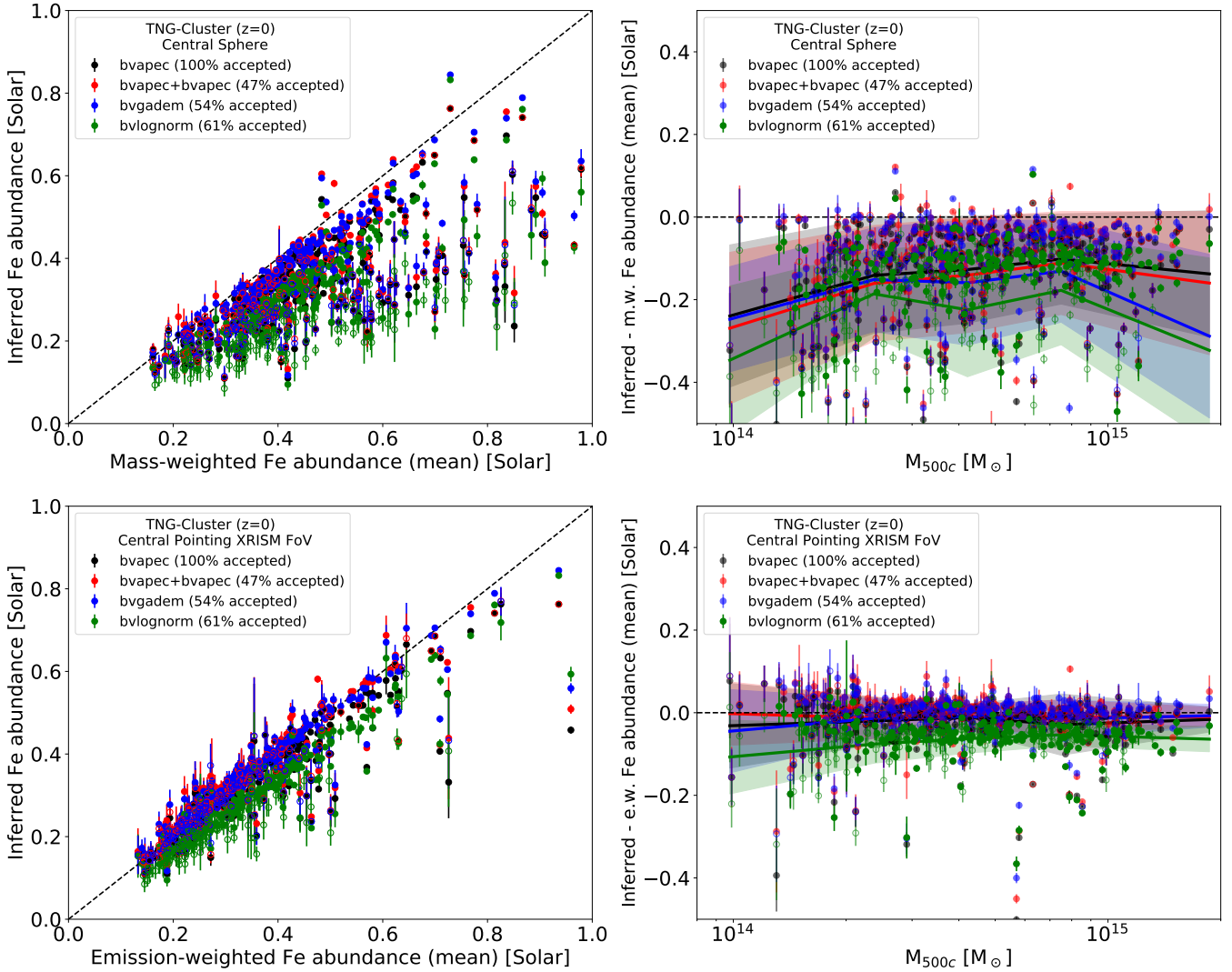


Figure 7. Observational inferences of the Fe abundance of the ICM at the centre of clusters. For the same spectral fits and modelling of Figure 5, we compare the Fe abundance inferred by all spectral-emission models used in this work to the true mean Fe abundance (left panels) of the input distribution: mass-weighted central gas (top) and emission-weighted gas for a central pointing with a *XRISM*-like FoV (bottom). Annotations are as in Figure 5 and, as there, we indicate the inference offset as a function of each cluster’s M_{500c} halo mass (right panels). Our results indicate that all models correctly infer the mean, emission-weighted Fe abundance of the gas in the FoV, with the exception of the *bvlognorm* model, which slightly but systematically underestimates it, being sensitive to the mass-weighted value instead. However, all inferences systematically underestimate the average true amount of Fe in the clusters’ centres.

spectral-emission model. This discrepancy disappears if we account for emission (bottom panels), suggesting it is possibly driven by less X-ray bright gas. Interestingly, even though the rejected fits do not occupy a special region in the parameter space, as in the temperature case, a disproportional amount of clusters appear to belong to this subset.

Similar to the case of the emission-weighted mean temperature, all models consistently trace the emission-weighted Fe abundance, or at least they trace more accurately the emission-weighted than the mass-weighted Fe abundance, with no significant halo-mass dependence. Only exception to this is the *bvlognorm*: the latter systematically underestimates the emission-weighted Fe abundance along the LoS, and it is in fact more sensitive to the mass-weighted value.

Overall, all models tend to underestimate the average Fe abundance of the gas in the centre of clusters. However, the single-point estimate for the amount of Fe is too simplistic of an approximation of the true, extended distribution. We speculate, for example, that extrapolating

this value throughout the entire volume could still systematically inflate the total amount of Fe in the ICM.

4 DISCUSSION

Overall, our results indicate that the assumptions on the temperature distribution of the gas may have an important impact on the inference of the properties of the ICM at the centre of clusters from X-ray spectral fitting, at least of those predicted by TNG-Cluster.

While the inferences from the *bvapec* model are comparable to (if not more accurate on average than) the rest, the model, by design, ignores the presence of multi-phase gas. Attempting to rectify this with the inclusion of another single-temperature component, in the form of the double *bvapec* model, does not improve the accuracy of the inferences on average (i.e. across the studied cluster sample) and actually returns a much larger fraction of clusters with very large

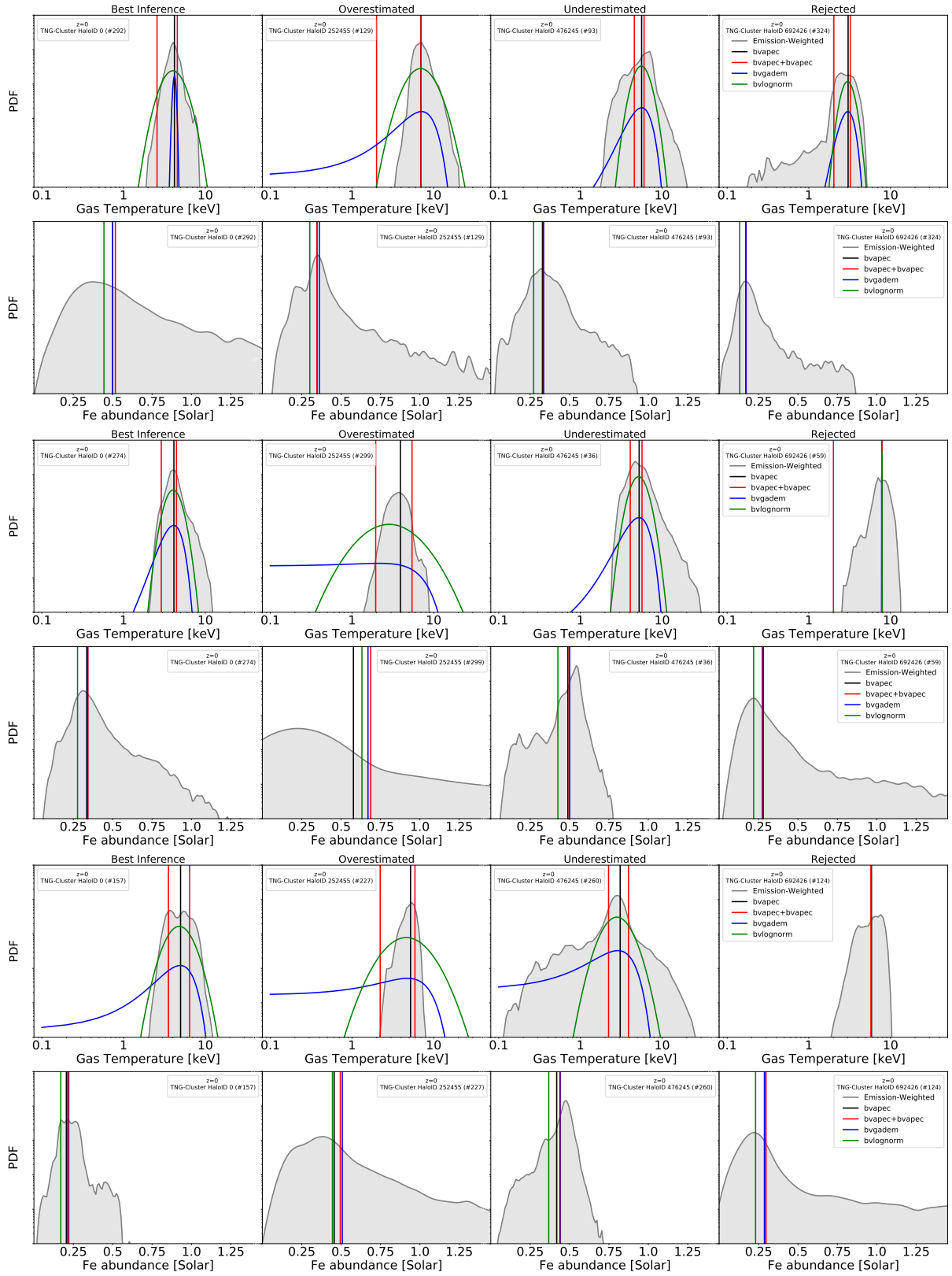


Figure 8. Observational inferences compared to the intrinsic gas cell distributions for a few TNG-Cluster examples. We present the true emission-weighted distributions of temperature and Fe abundance of the gas cells for a central pointing with a *XRISM*-like FoV from TNG-Cluster in grey as they compared to the outcome of X-ray fitting via each of the spectral-emission models studied in this work. The individual example clusters shown in this Figure are selected based on the quality of the *bvlognorm* inference w.r.t. the mean of the temperature (top), mean Fe abundance (bottom) and the best-fit Log-Normal distribution width (middle). For each case we showcase a system with a best, an overestimated and underestimated inference, from left to right. A case of a rejected fit with a reasonable inference is also shown as a comparison (rightmost column). Our results highlight the strength and weaknesses of each model in providing an accurate representation of the complex input distributions of the gas in clusters (see text for details). This Figure also provides examples whereby the lack of constraints on the breadth of the ICM temperature distribution as the main factor behind rejection of both *bvgadem* and *bvlognorm* models.

inference errors on the ICM effective temperature, with biases in both directions.

The `bvgaDEM` and `bvlognorm` assume a Normal and Log-Normal distribution of temperatures, respectively, hence allowing a more complete description of the properties and diversity of the gas at the centre of clusters. For this reason, they return somewhat more frequently successful fits than the double `bvapeC` model. And for the same reason, we argue that they should be prioritized, especially when attempting to study complex phenomena such as the effects of AGN feedback on the ICM, which could impact different gas phases differently (as is the case in the TNG model, see e.g. [Truong et al. 2024](#)). However, on average, the `bvgaDEM` and `bvlognorm` models do not necessarily return more accurate inferences of the ICM effective temperature and average Fe abundance. And, as shown, they too slightly albeit systematically underestimate the bulk properties of the ICM that is actually located close to the cluster centre.

In the following sections, we compare the fits produced by each model to the simulation-intrinsic distributions, in order to examine the quality of each inference in greater detail. We also investigate the impact that projection effects and brightness bias have on the inference of the properties of the central gas, in order to understand the systematic offsets between the two quantified so far. Finally, we also attempt to account for selection biases, such as focusing only on the X-ray brighter strong cool-core (SCC) clusters, in order to make our results more applicable to typical observational approaches.

4.1 Insights on the quality of the observational inferences, and of the fits, across spectral-emission models

As we have previously shown, all the spectral-emission models used in this work are capable of inferring with good accuracy the emission-weighted summary statistics of the cluster gas from a central pointing with a XRISM-like observation. Yet, for a large number of clusters, they fail to return an accepted best fit of the underlying X-ray spectrum. Moreover, as mentioned above and by comparing the filled and empty markers of [Figure 5](#), [Figure 6](#) and [Figure 7](#), it would appear that the rejection of the X-ray spectra fits (at least based on our criteria, see [subsection 2.3.1](#)) does not translate in much or overall worse inference errors. This can be appreciated via the quantitative summaries provided in [Table A1](#) and [Table A2](#). In the following, we hence provide further considerations as to why the quality of the fit may still be relevant when choosing which spectral-emission model to adopt to analyse the data.

4.1.1 Examples of true vs. inferred gas distributions

In [Figure 8](#) we showcase the *emission-weighted* distributions of the ICM properties of a few example individual systems in comparison to their best-fit description, for all the spectral-emission models studied in this work. Each cluster is represented by two panels, one for temperature and one for Fe abundance, respectively, on top of each other. We show a total of 12 example clusters, selected based on the performance of the `bvlognorm` model to infer, respectively, effective temperature (top two rows), Fe abundance (bottom two rows) and temperature width (middle two rows). We focus on the `bvlognorm` because it is the best descriptor of the TNG-Cluster temperature distributions ([Figure 3](#) and [Figure 4](#)).

From left to right, we visualize the intrinsic and inferred gas property distributions for different example cases. In the leftmost column, we show systems with the minimum absolute difference between the true and inferred value of the relevant property. We also showcase

instances of an overestimation and underestimation, located at the 95th and 5th percentile of the sorted difference distribution, respectively (middle columns). Finally, we also show examples of rejected fits (rightmost column), so that we can better understand the intrinsic properties of the gas that, despite an accurate inference, led to model rejection.

Starting with the accepted spectral fits, we can understand how each model attempts to infer the input temperature distribution. The double `bvapeC` model (red lines) systematically infers temperatures that are not present or not associated with any minor peaks in the temperature distribution. Similarly, in many cases it fails to identify the most prominent peak, by inferring two temperatures around it. This suggests that the model, in an attempt to approximate a distribution of temperatures, does not provide an accurate representation of the actual distribution but an attempt of residual minimisation.

The `bvgaDEM` model (blue lines) can provide a good approximation of distributions extended towards higher temperatures, but systematically assumes a much larger amount of cooler gas compared to what is present. Finally, many cases show how the `bvlognorm` model provides a fairly accurate representation of the width of the temperature distributions. However, it tends to fail when the intrinsic thermal structure deviates strongly from a Log-Normal distribution in the form of extended tails towards higher- or lower-temperature gas.

Regarding the Fe abundance distributions, all spectral-emission models make overly simplistic approximations. We see a range in the capability of all models to identify the Fe abundance of the majority of the gas, with the `bvlognorm` model inferring lower values compared to the other models. This behaviour is consistent with our results above, where the models appear more sensitive to the mean values.

Another important aspect regarding the inference of each model are the conditions that led to its rejection. As we can see in [Figure 8](#) and as previously indicated in [Figure 5](#) and [Figure 7](#), the rejected fits of all models do infer a fairly accurate value of the mean temperature and Fe abundance emission-weighted distribution. For `bvgaDEM` and `bvlognorm`, the main and most frequent factor that leads to the rejection of the model is the width of the distribution: in some rejected cases, the inferred width is simply too large, infinity; in other rejected cases, the model infers a very narrow temperature distribution, i.e. with a poor constraint on the width itself.

4.1.2 Dependence of quality of the fit on number of photons

Considering the sensitivity of all models on the emission-weighted properties of the gas along the LoS, it is possible that a model cannot infer the temperatures of the less luminous gas contributing to the distribution because of a lack of counts.

In [Figure 9](#) we examine this hypothesis by comparing each model inference on the temperature and Fe abundance as a function of the number of counts. It is evident from the distribution of our clusters that the rejected `bvlognorm` best-fits tend to have systematically lower counts than the accepted ones, but the count distributions of the two populations have a significant overlap. We note that the same behaviour holds for the accepted and rejected best-fits of the other spectral emission models.

To understand the extent that exposure time may have on the rejection of our best-fits, we repeat the X-ray spectra mocking and analysis for the rejected clusters by increasing the exposure time to 300 ks, instead of the fiducial 100 ks adopted throughout. For the case of the `bvlognorm` model (which returns the largest success rate), we find that 54 per cent of the clusters that have been previously rejected turn out to have a valid fit with an increased exposure (not shown).

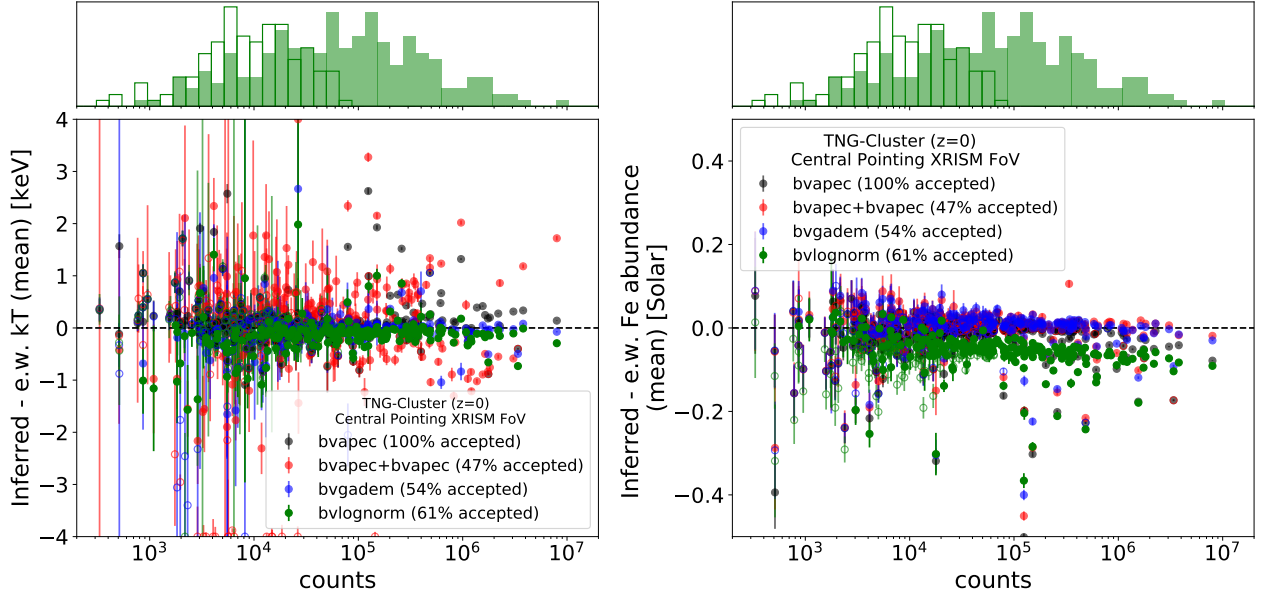


Figure 9. Inferring the ICM temperature and Fe abundance, across spectral-emission models, as a function of detected photons per cluster. We present the quality of each model’s inference on the emission-weighted mean temperature (left) and Fe abundance (right) of the gas as a function of the number of counts observed for a 100 ks exposure. As previously, we consider all the ICM for a central pointing with a *XRISM*-like FoV. The black dashed line represents unity. We present the accepted and rejected fits with filled and open symbols, respectively. In the two top subplots, we also show the distribution of photon counts per clusters for the accepted (filled) and rejected (empty) *bvlognorm* best fits. Our findings indicate that the best fits of fainter clusters tend to be more likely to be rejected, suggesting a correlation between acceptance and X-ray brightness, and even if rejected and accepted fits seem to return similarly-accurate results across the cluster sample

This confirms the hypothesis that the rejection of a spectral fit for the fainter clusters in our sample is due to available exposure time.

However, this is not just a cluster-mass effect, as in fact there still remains a population of systems for which the best-fit is still rejected, even though their inferences on the emission-weighted mean temperature and Fe abundance are comparable with the rest of the sample. We find (although do not show) that clusters that are rejected even for a three-time longer exposure are metal poor, with the majority of the emission-weighted mass in the ICM having an Fe abundance of ~ 0.25 Solar – such average spans between 0.15 and 0.9 Solar across the whole TNG-Cluster systems, e.g. Figure 7, bottom left panel.

This is probably due to the fact that the spectral-emission models use the emission lines also to recover the thermal distribution of the gas. Whereas the shape of the continuum is a reliable diagnostic of the ICM’s bulk temperature, for plasma with temperatures higher than 2 keV, the emission-line ratios trace the presence of cooler or hotter gas, constraining the width of the distribution. However, if clusters have low elemental abundances, they will return low numbers of counts in spectral lines irrespective of the longer exposures, and in turn the modelling will be unable to provide any meaningful constraints on the width of the thermal distribution, leading to their rejection.

Overall this indicates that even the more accurate assumption of a Log-Normal temperature distribution is not a sufficient representation of the properties of the ICM, as predicted by TNG-Cluster, both for its thermal and more importantly its chemical structure. This highlights the limitations of current spectral emission models and the need for more sophisticated descriptions of the intrinsic properties of the gas in order to better understand the ICM.

4.2 Effects of observational realism

Although it may be assumed in observations-based works that the observed spectra are representative of the de-projected, local conditions of the ICM that a telescope is pointing at, our analysis above suggests that there are systematic biases between the true mass-weighted state of the ICM that truly resides at the centre of clusters and the emission-weighted summary statistics of all the ICM gas that contributes to the signal from a central-pointing observation: see differences in the inference errors between top and bottom panels of e.g. Figure 5 and Figure 7. We now explore the individual sources of those differences and quantify their impact and systematic uncertainties. For the purposes of this analysis we focus again exclusively on the *bvlognorm* model as a reference point. However, the qualitative effects that we find are consistent across all models.

4.2.1 Projection effects

In observations, all gas in projection along the line-of-sight (LoS) contributes to the observed spectra, even though it may not be associated with the central ICM that we are interested in here. Previous works using simulated clusters have shown that projection effects can lead to severe misinterpretations of the intrinsic thermal and chemical properties of the ICM due to the gas along the LoS (e.g. Zhang et al. 2024; Štofanová et al. 2024). In order to quantify the impact of the projected gas in our work we compare the mass-weighted distributions of all the cluster gas in a central pointing with a *XRISM*-like FoV to the mass-weighted distribution of the gas cells that actually reside in the region of interest, in this case a sphere of a 33.5 kpc radius located in the centre of each cluster.

In Figure 10, we compare the thermal structure of the gas in the centre to the total gas observed in our mocks (top right), and

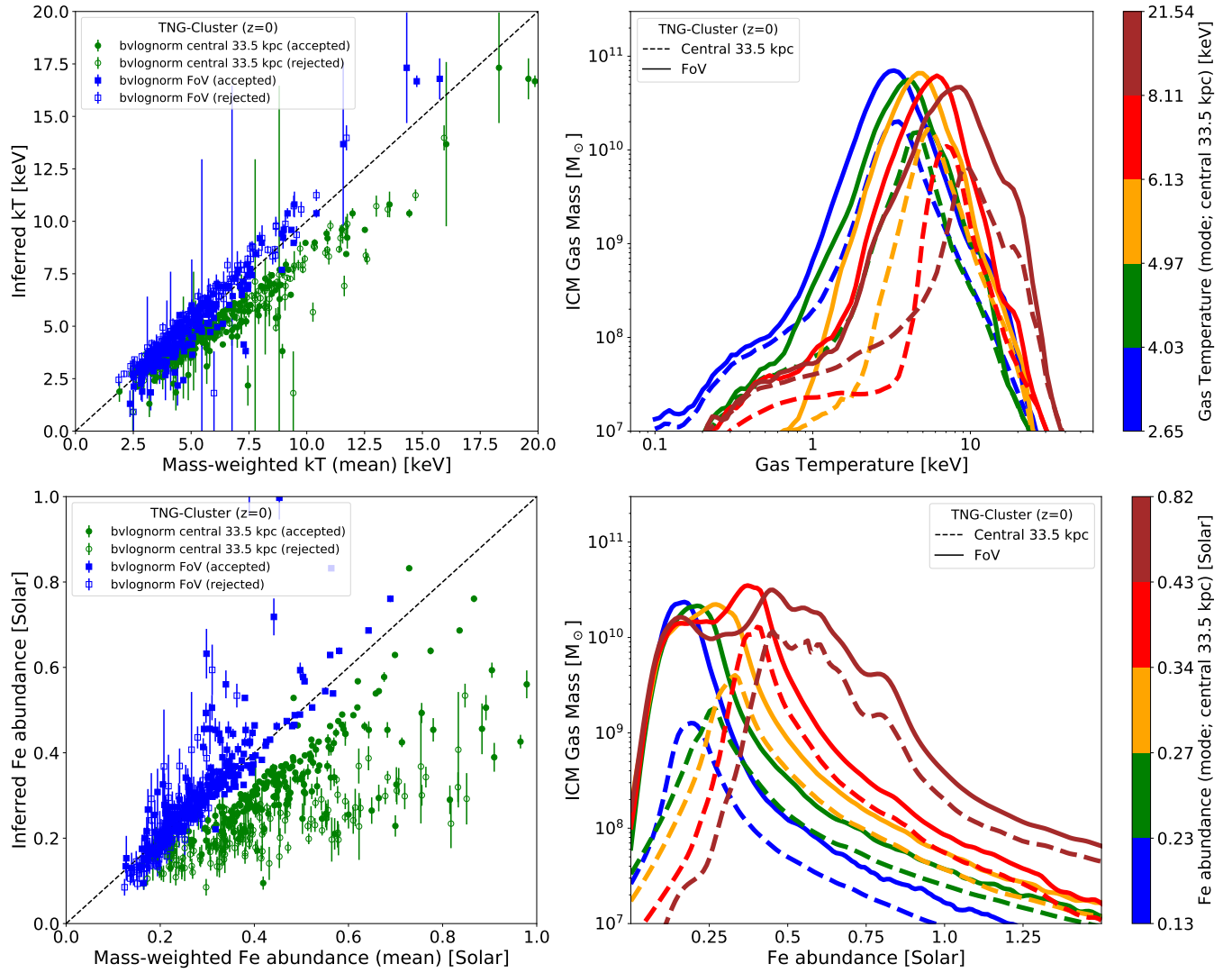


Figure 10. Systematics due to projection effects in the temperature (top) and Fe abundance (bottom) distributions. We highlight the impact of projection effects on the observational inferences, by comparing the *bvlognorm* best-fit outcome to the true mass-weighted mean temperature of the central (green) vs. projected (blue) gas (left). The latter includes all gas for a central pointing with a *XRISM*-like FoV but, differently than in previous Figures, without weighting by X-ray emission. The black dashed line represents unity. We also plot the respective average mass-weighted and KDE-smoothed temperature and Fe abundance distributions, binned w.r.t. the mode of the central gas distribution (right panels) – this allows us to better illustrate changes in their shape. Our results indicate that the systematic underestimation of the central ICM properties is primarily driven by projection effects, which, by introducing cooler and less abundant gas in the LoS, bias low both the temperature and Fe abundance inferences.

their corresponding inference errors (top left). Since the temperature distribution of the gas in the cluster centre can be approximated by a unimodal distribution, we bin the clusters in percentiles based on the mode of their temperature distribution. In fact, due to the tight correlation between ICM temperature and the halo mass, the temperature bins of Figure 10 top right are comparable to mass bins. Differently than e.g. in Figure 5, here we isolate the effects of projections alone, by comparing directly mass-weighted vs. mass-weighted quantities rather than mass-weighted vs. emission weighted ones.

We see that the projection of gas from larger radii along the LoS shifts the temperature distribution towards lower temperatures (dashed vs. solid curves), due the projection of cooler gas from the outskirts of the cluster. The effect is more pronounced for systems with higher ICM temperature, or equivalently higher halo mass, due to the stronger temperature gradient up to R_{500c} in those systems.

This is consistent with the strong dependence of the temperature inference on halo mass, found in Figure 5. By comparing the difference between the inferred temperature with the *bvlognorm* model on the one side and the the mean, mass-weighted temperature of the central vs. LoS gas, we find much larger inference errors in the former case, with average offsets of -1.2 keV (-18 per cent) and 0.16 keV (3 per cent), respectively, with a strong dependence on halo mass. Given that, on average, the inferred ICM effective temperature differs by -1.2 keV from the true one (Figure 5, and Table A1), we can conclude that projection effects dominate the observational bias.

Due to the projection of cooler gas, the width of the distribution systematically increases for all systems, but the effect shows a similar positive correlation with halo mass, being more pronounced for the most massive systems. While the increase is asymmetric, i.e. primarily for cooler gas, the tails of sub-keV gas remain unaffected overall, highlighting their central origin. However, with or without projected

gas, the capability of the `bvlognorm` model to accurately return the true width of the input distribution remain unchanged (not shown).

Projection effects are far more influential on the chemical structure of the ICM. In [Figure 10](#) (bottom) we show the mass-weighted Fe abundance distributions of both central and projected gas. Similar to the temperature distributions, we bin the clusters based on the mode of the central gas, as it consists of one prominent peak. However, unlike the temperature of the ICM, TNG-Cluster shows no clear correlation between halo mass and metal enrichment. Our results indicate that, due to projection effects, a multitude of additional abundance peaks appear in the mass-weighted Fe abundance distribution of the gas across the LoS. These peaks consist of less metal-enriched gas and are more prominent in the systems with a higher core enhancement, since for the less enriched clusters the Fe abundance distribution remains effectively unimodal. The effect arises from large amounts of less-enriched gas that is located at larger galactocentric radii intersecting the LoS, which hence biases the mean Fe abundance low. Namely, projection effects change an average inference errors between the `bvlognorm` inferred metallicity and the intrinsic mass-weighted mean Fe abundance from -0.18 Solar (-28 per cent) for the central gas to 0.02 Solar (7 per cent) for the full column. The effect has a strong dependence on the mean Fe abundance of the ICM, but it is independent of halo mass, explaining the trend we see in [Figure 7](#).

4.2.2 Brightness biases

Previous studies have shown that observed ICM values are more related to emission-weighted properties than to e.g. mass-weighted properties (e.g. [Biffi et al. 2017, 2018](#)). An emission spectrum, and models to fit emission spectra, are necessarily sensitive in a weighted way towards the most luminous gas, rather than the entire mass of the ICM. We therefore quantify this bias due to brightness by comparing the mass- and emission-weighted distributions of the gas along the LoS, as well as how it influences inferences by the `bvlognorm` model.

Starting with the thermal structure, [Figure 11](#) shows the difference between emission and mass weighted distributions (top right). Overall, these are small, and primarily visible in the sub-keV tails. This is expected as the associated gas is located close to the cluster centre, is densest, and is therefore brighter than most other gas along the line of sight. The influence on the quality of the `bvlognorm` inference is similarly mild (top left). We find a shift from an average inference error of 0.16 keV (3 per cent) to -0.08 keV (-1 per cent) from the mass-weighted to the emission-weighted ICM effective temperature.

The effect is more significant for the inference of the width of the temperature distribution and yet the brightness bias does not seem to justify the differences in inference errors between the top and bottom panels of [Figure 6](#) (not shown).

Finally, in [Figure 11](#) (bottom) we examine the effects of the brightness bias on the Fe abundance distribution (bottom right). Similar to the temperatures, by favouring the brightest gas along the line of sight, there is an enhanced contribution from the super-Solar tails, that are associated with the cluster centre, and a relatively suppressed contribution from gas in the outskirts of the cluster. As a result, the emission-weighted mean Fe abundance is biased high, resulting in an average inference error of -0.06 Solar (-18 per cent) compared to the average 0.02 Solar (7 per cent), inferred by the `bvlognorm` model for the mass-weighted case.

Overall, for central pointings, the brightness bias has a minimal influence on the accuracy of the observational inferences on the properties of the projected gas. This could become more a significant issue for off-centre pointings, where the projected gas becomes compara-

ble to the medium that is targeted. Examining and quantifying the influence of those biases in such cases is left for a future study.

4.3 Selection effects: i.e. the case of cool-core clusters

In our analysis, we have been considering the entire sample of 352 clusters in TNG-Cluster at $z = 0$. However, samples of observed clusters tend to not be as diverse, due to selection effects. For example, many of the clusters in the literature are cool core (CC), as they are significantly brighter than their non cool-core (NCC) counterparts and considered the best targets for the study of AGN feedback. Therefore, we now investigate if the inferences of our models depend on the cool-core state of a cluster.

In [Figure 12](#) we present the offsets between inferred and mean, mass-weighted temperature and Fe abundance for the gas in the centres of our clusters, as a function of their central cooling time and central entropy (from [Lehle et al. 2024](#)). For both cases, we find no strong correlation between the inference error and the cool core metric, although the scatter is larger for NCC clusters.

Regarding the rejected best-fits, while a number of CC clusters fail to produce an accepted fit for all models, the rejected fits disproportionately arise from the NCC subsample. This is also evident in the spectral fit acceptance rates, as the CC cluster subsample outperforms the general population. As previously shown, constraining the temperature distribution depends on the number of counts and therefore it can be more easily accomplished the brighter the associated gas is.

Finally, we examine the associated observational inferences on the properties of the ICM, if our sample of clusters consists only of the brightest (CC) clusters. Selecting only for the systems with central cooling times below 1 Gyr (following [Lehle et al. 2024](#)), we examine their impact on temperature and Fe abundance.

In [Figure 13](#) we show the distribution of the CC clusters versus the full sample (shown in [Figures 5 and 7](#), for comparison). For both the temperature and Fe abundance, the average inference error increases or remains similar to that of the entire sample, respectively. For example, for the accepted `bvlognorm` fits, the change is from -1.14 keV (-18 per cent) to -0.69 keV (-14 per cent) and from -0.15 Solar (-25 per cent) to -0.12 Solar (-23 per cent) for the mean, mass-weighted temperature and Fe abundance, respectively. However, excluding the faintest objects does remove the majority of the outliers, suggesting that the least accurate inferences occur for NCC clusters.

5 SUMMARY AND CONCLUSIONS

In this paper, we have used the outcome of TNG-Cluster, a cosmological magnetohydrodynamical simulation of 352 massive clusters and their galaxies, to assess the accuracy with which it will be possible to infer the temperature and metallicity of clusters' centres via high-resolution X-ray spectroscopy.

To this end, we have quantified the thermal and chemical properties of the ICM at the centre of TNG-Cluster systems at $z = 0$ and we have developed an end-to-end pipeline to generate and analyse synthetic X-ray spectra that could be obtained with *XRISM/Resolve*-like observations targeting the core regions of clusters at $z \sim 0$. We have hence quantified the ability of commonly-used spectral-emission models (`bvapec`, `double bvapec`, `bvgadem`, and `bvlognorm`) to recover the intrinsic temperature distribution and Fe abundance of the gas.

Our main results are as follows:

- TNG-Cluster predicts broad distributions for both temperature

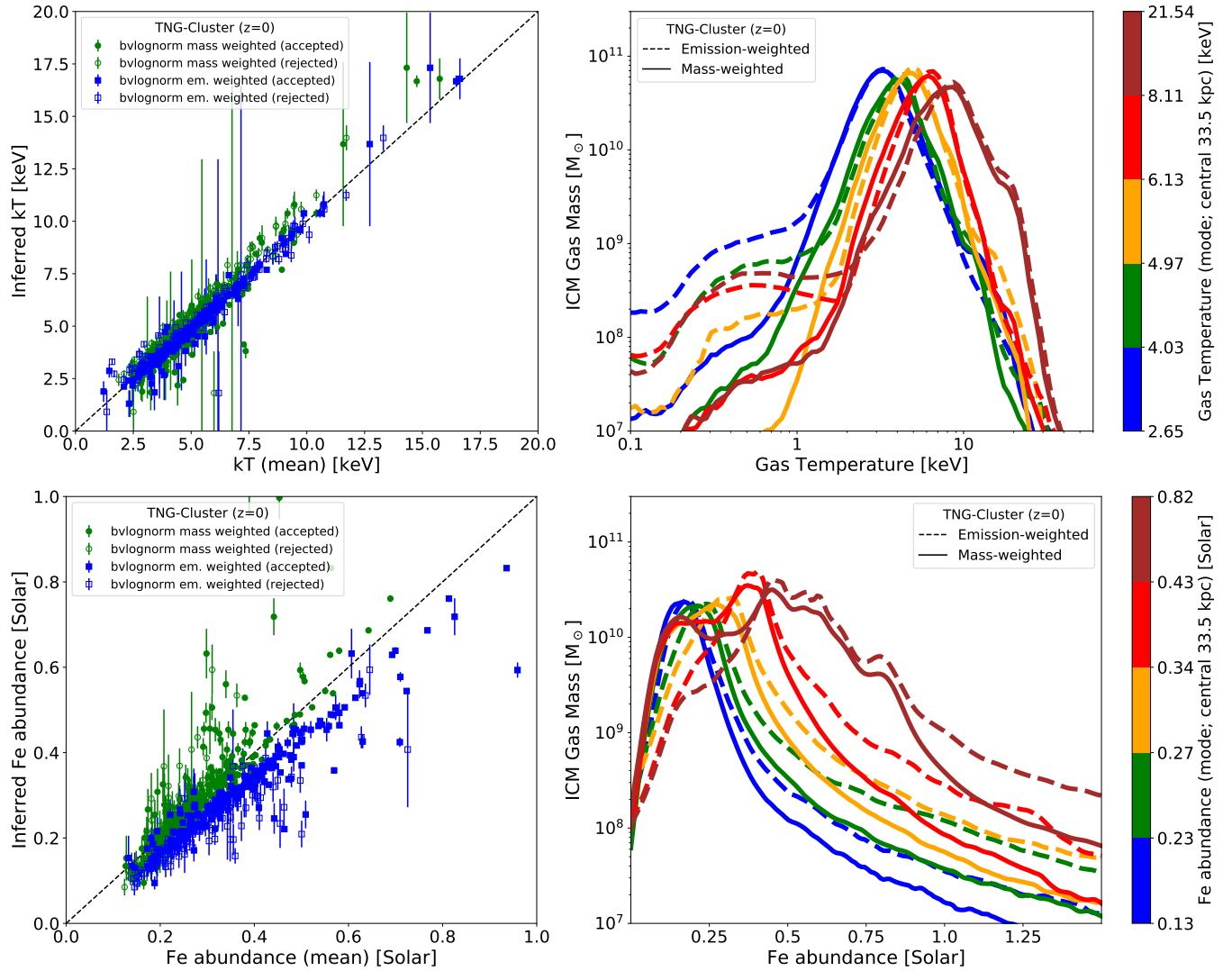


Figure 11. Systematics due to the brightness bias in the temperature (top) and Fe abundance (bottom) distributions. We quantify the impact of the brightness bias on the observational inferences by comparing the `bvlognorm` best-fit results to the true mass- (green) and emission-weighted means (blue) of the gas contributing to a central pointing with a *XRISM*-like FoV. In the right panels, we also plot the respective average mass-weighted (solid) and emission-weighted (dashed) KDE-smoothed temperature and Fe abundance distributions, binned by the mode of the central gas distribution (different colors). Our results indicate that the emission-weighted quantities overestimate the relative contribution of the sub-keV and super-Solar gas close to the cluster centre, in turn biasing high the average Fe abundance but with minimal influence on the mean temperature.

and Fe abundance for the gas in the centres of clusters, with a large cluster-to-cluster variation even across systems with similar total halo mass (subsection 3.1, Figure 2).

- The intrinsic temperature distribution of the gas in the centre of clusters, both mass-weighted and emission-weighted, is best approximated by a Log-Normal (rather than a Normal) functional form, even if the best-fit Log-Normal description that does not fully capture the sub-keV gas tails that can be present in some, but not all, clusters (subsection 3.1, Figure 3 and Figure 4).

- The central ICM temperature inferred via all spectral-emission models is consistent with the true emission-weighted average along the line of sight, but systematically underestimates the mass-weighted temperature of the gas that is truly located in the clusters centre. This inference bias reads, on average (i.e. across the whole population of 352 clusters), -1.2 keV (-18 per cent), so it is arguably small, but has a strong dependence on halo mass (subsection 3.2, Figure 5). For $10^{15} M_{\odot}$ clusters, all spectral-emission models return mean

temperatures that are smaller by 2 keV, on average, than the true average one.

- The width of the temperature distribution inferred by the `bvlognorm` model, is, on average, consistent with the true mass-weighted distribution of the central ICM, but systematically underestimates the breadth of the emission-weighted distributions. In contrast, the `bvgadem` model overestimates the width of both mass- and emission-weighted temperature distributions (subsection 3.2, Figure 6).

- The inferred Fe abundance is consistent with the true mean, emission-weighted Fe abundance of the gas along the line of sight, i.e. for a central pointing with a *XRISM*-like FoV. The `bvlognorm` model is closest to the mass-weighted value. However, all models similarly underestimate the mean Fe abundance in the cluster centre by about 0.11 Solar (21 per cent) (subsection 3.3, Figure 7).

- The rejection of fits of the X-ray spectra correlates with the number of collected photon counts. More than half of the initially rejected

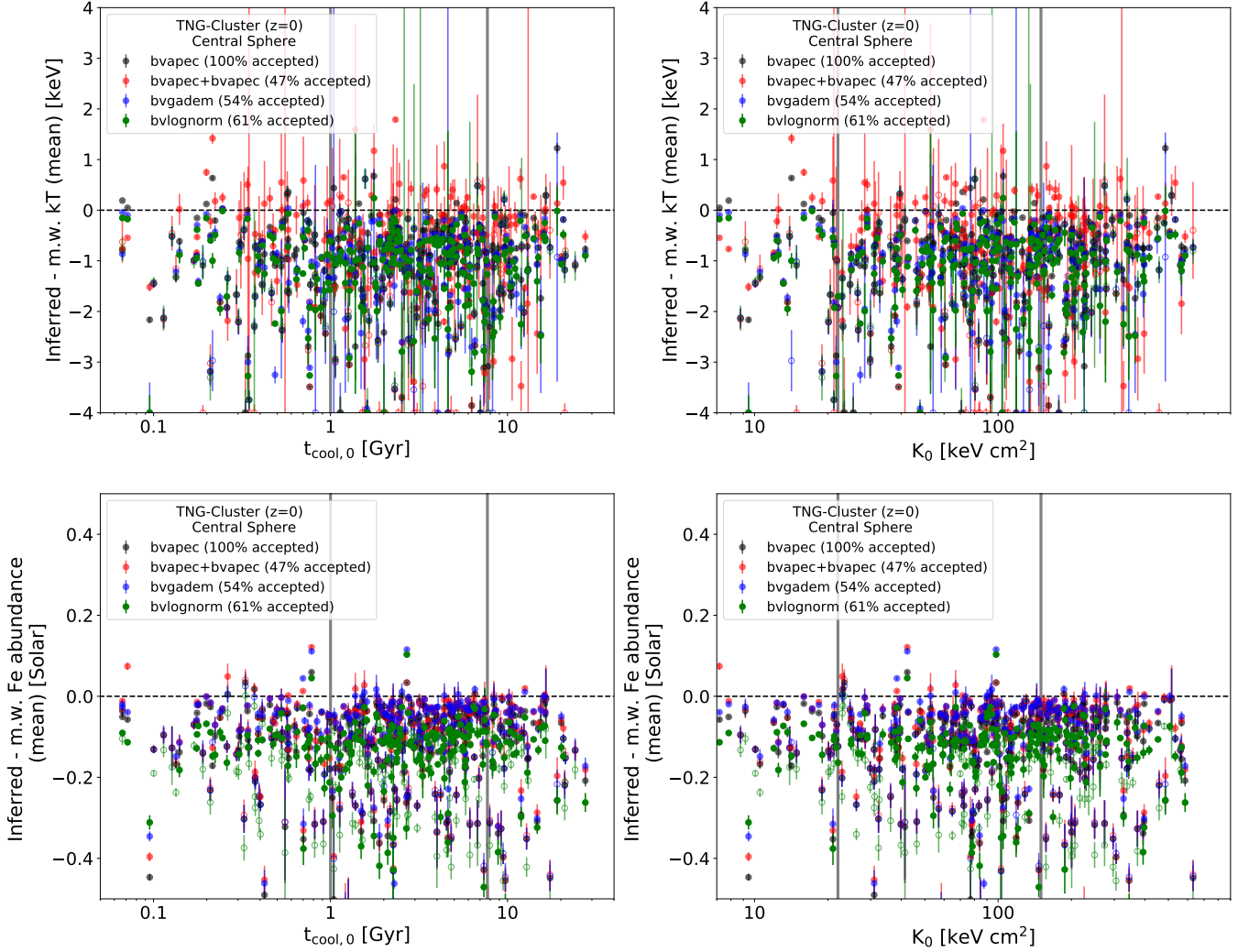


Figure 12. Observational inferences of the properties of the ICM at the centre of clusters as a function of cool-core criteria properties. In the top (bottom), we present the offsets between inferred temperature (Fe abundance) and the true mass-weighted mean of the central gas as a function of the cooling time (left) and central entropy (right) inside the $0.012 R_{500c}$. The horizontal dashed line represents unity, while the vertical thick solid lines indicate strong cool-core (SCC) vs. weak cool-core (WCC) vs. non-cool-core (NCC) thresholds (see text). We see no clear trends between the inference errors and the clusters' core properties, even if the cluster-to-cluster variations are smaller for strong CCs.

bvlognorm fits do succeed with longer exposure times. However, a subsample of metal-poor systems fail to produce an accepted spectral fit, despite this longer exposure (300ks vs 100ks; [subsection 4.1, Figure 9](#)).

- Projection effects are the primary reason of the offset between inferred and the actual properties of the central ICM. In contrast, the brightness bias (emission- vs. mass-weighted) has a smaller impact, at least for central pointings ([subsection 4.2, Figure 10, Figure 11](#)).

- When considering only strong cool-core clusters, as is the case in many observational samples, model inferences on central ICM temperature improve only marginally (with e.g. inference errors of 0.7 keV on average compared to 1.2 keV across a randomly-selected overall sample). The CC-selection effect on the inference of Fe abundance is even smaller. The main advantage of selecting for SCCs is the removal of strong outliers, i.e. of clusters for which the observational inferences of ICM properties are catastrophically wrong ([subsection 4.3, Figure 13](#)).

Overall, our analysis highlights the importance of properly mod-

elling the complex temperature and metallicity distributions of the ICM at the centre of clusters. The different spectral-emission models that we have considered have different strengths and weaknesses, or practical justifications. Barring the double bvapec, which returns highly inaccurate results for more clusters than the other models, all studied assumptions return overall similarly accurate inferences of the effective temperature and average metallicity of the ICM at the centre of clusters. However, based on the predictions of TNG-Cluster, we recommend to use models that allow for a temperature distribution, as both single and double temperature models simply fail at capturing the diversity and complexity of the ICM. Similarly, the single-value Fe-abundance assumption, typical of all ICM X-ray spectra analyses, seems utterly inadequate to represent the multifacetedness of the ICM enrichment, even in the innermost regions of clusters – a qualitative shift in the way ICM X-ray spectra are fitted for, and hence interpreted, seems of the essence. Finally, due to the large influence of the effects associated with observational realism, particularly projection effects, a careful deprojection to the 3D properties of the gas from observed data is required.

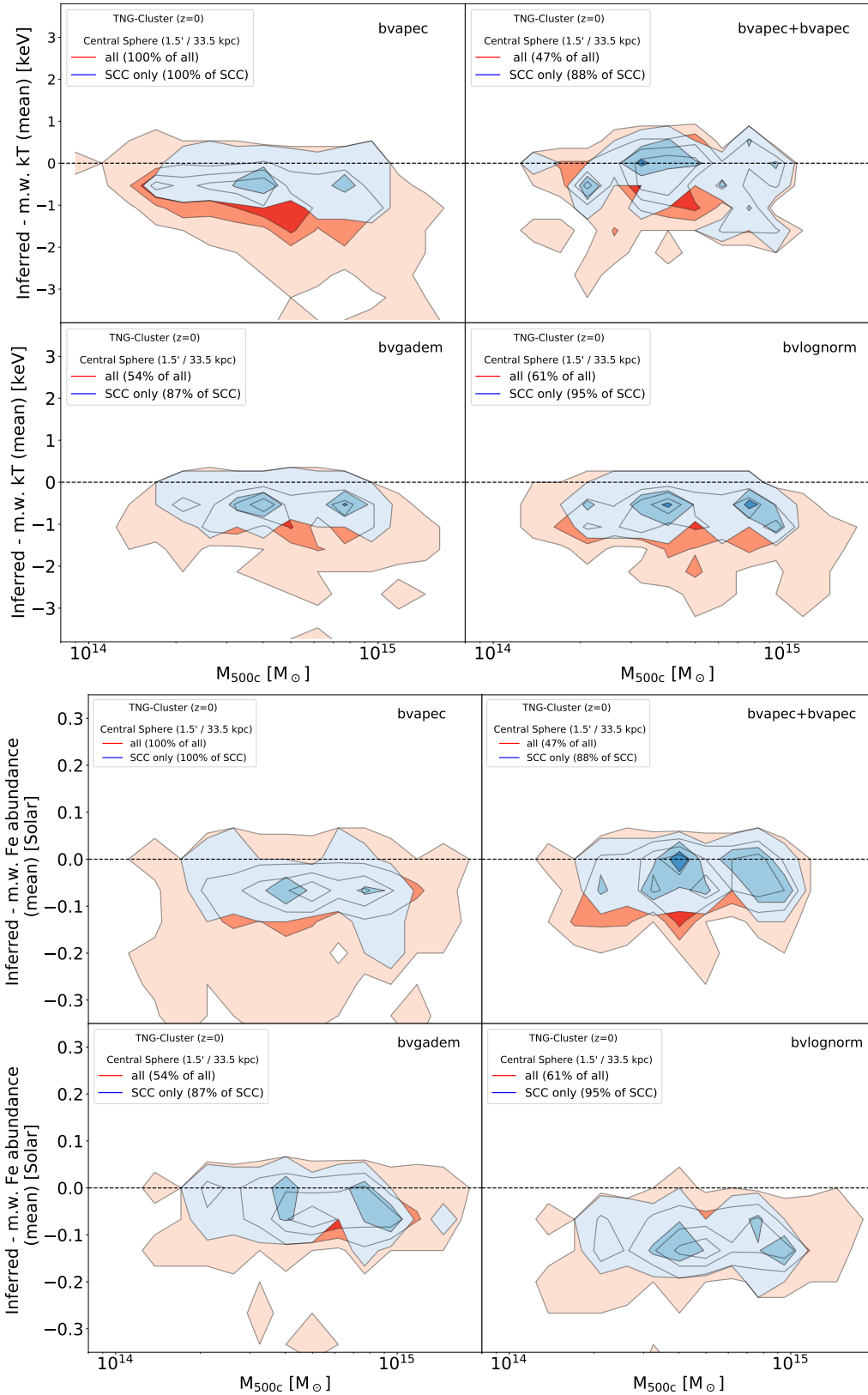


Figure 13. Are there classes of clusters, such as cool-core clusters, for which the observational inference errors of the central ICM properties are smaller? We focus on ICM effective temperature (top) and the Fe abundance (bottom) of the central gas and compare the inference errors as a function of total cluster mass for all TNG-Cluster systems (orange shaded areas and contours) to those of only strong cool cores (blue shaded areas and contours; see text for details). For the former, the results are identical to those shown in Figure 5 and Figure 7. Our results show that selecting only for SCCs in our sample does not change the average systematic offsets, but does remove the majority of outliers.

While we have primarily focused on the ICM Fe abundance, in future work we will assess the accuracy of *XRISM/Resolve*-like observations and analyses in recovering the abundances of other metal species, in addition to gas kinematics. It remains to be quantified how the figures put forward here translate to lower, CCD-like resolution spectra, such as with *XMM-Newton*, to observations targeting off-centre pointings and cluster outskirts, and to science cases that rely on spatially-resolved analyses.

DATA AVAILABILITY

All the output of the TNG-Cluster simulation is now publicly available, as are the IllustrisTNG simulations: see www.tng-project.org/data and Nelson et al. (2019). The data generated in this project, including *XRISM* Resolve mocks, spectra, and spectral-fitting results, will be made available upon acceptance.

ACKNOWLEDGEMENTS

DC is a fellow of the International Max Planck Research School for Astronomy and Cosmic Physics at the University of Heidelberg (IMPRS-HD) and, together with AP, acknowledges funding from the European Union (ERC, COSMIC-KEY, 101087822, PI: Pillepich). DN acknowledges funding from the Deutsche Forschungsgemeinschaft (DFG) through an Emmy Noether Research Group (grant number NE 2441/1-1).

The TNG-Cluster simulation suite has been executed on several machines: with compute time awarded under the TNG-Cluster project on the HoreKa supercomputer, funded by the Ministry of Science, Research and the Arts Baden-Württemberg and by the Federal Ministry of Education and Research; the bwForCluster Helix supercomputer, supported by the state of Baden-Württemberg through bwHPC and the German Research Foundation (DFG) through grant INST 35/1597-1 FUGG; the Vera cluster of the Max Planck Institute for Astronomy (MPIA), as well as the Cobra and Raven clusters, all three operated by the Max Planck Computational Data Facility (MPCDF); and the BinAC cluster, supported by the High Performance and Cloud Computing Group at the Zentrum für Datenverarbeitung of the University of Tübingen, the state of Baden-Württemberg through bwHPC and the German Research Foundation (DFG) through grant no INST 37/935-1 FUGG. The material is based upon work supported by NASA under award number 80GSFC24M0006.

All the analysis and computations associated to this paper have been realized on the Vera cluster of the MPCDF.

REFERENCES

- Allen S. W., Evrard A. E., Mantz A. B., 2011, *ARA&A*, 49, 409
 Arnaut K. A., 1996, in Jacoby G. H., Barnes J., eds, *Astronomical Society of the Pacific Conference Series Vol. 101, Astronomical Data Analysis Software and Systems V*. p. 17
 Asplund M., Grevesse N., Sauval A. J., Scott P., 2009, *ARA&A*, 47, 481
 Ayromlou M., et al., 2024, *A&A*, 690, A20
 Biffi V., et al., 2017, *MNRAS*, 468, 531
 Biffi V., Planelles S., Borgani S., Rasia E., Murante G., Fabjan D., Gaspari M., 2018, *MNRAS*, 476, 2689
 Chadayammuri U., Eisert L., Pillepich A., Lehle K., Ayromlou M., Nelson D., 2024, *arXiv e-prints*, p. [arXiv:2410.22416](https://arxiv.org/abs/2410.22416)
 Foster A. R., Ji L., Smith R. K., Brickhouse N. S., 2012, *ApJ*, 756, 128
 Gastaldello F., Simionescu A., Mernier F., Biffi V., Gaspari M., Sato K., Matsushita K., 2021, *Universe*, 7, 208

- Ghirardini V., et al., 2024, *A&A*, 689, A298
 Hitomi Collaboration et al., 2017, *Nature*, 551, 478
 Kalberla P. M. W., Burton W. B., Hartmann D., Arnal E. M., Bajaja E., Morras R., Pöppel W. G. L., 2005, *A&A*, 440, 775
 Kawahara H., Suto Y., Kitayama T., Sasaki S., Shimizu M., Rasia E., Dolag K., 2007, *ApJ*, 659, 257
 Khedekar S., Churazov E., Kravtsov A., Zhuravleva I., Lau E. T., Nagai D., Sunyaev R., 2013, *MNRAS*, 431, 954
 Kravtsov A. V., Borgani S., 2012, *ARA&A*, 50, 353
 Lee W., Pillepich A., ZuHone J., Nelson D., Jee M. J., Nagai D., Finner K., 2024, *A&A*, 686, A55
 Lehle K., Nelson D., Pillepich A., Truong N., Rohr E., 2024, *A&A*, 687, A129
 Marinacci F., et al., 2018, *MNRAS*, 480, 5113
 Mernier F., et al., 2018, *Space Sci. Rev.*, 214, 129
 Mernier F., et al., 2023, *arXiv e-prints*, p. [arXiv:2310.04499](https://arxiv.org/abs/2310.04499)
 Naiman J. P., et al., 2018, *MNRAS*, 477, 1206
 Nelson D., et al., 2018, *MNRAS*, 475, 624
 Nelson D., et al., 2019, *Computational Astrophysics and Cosmology*, 6, 2
 Nelson D., Pillepich A., Ayromlou M., Lee W., Lehle K., Rohr E., Truong N., 2024, *A&A*, 686, A157
 Pillepich A., et al., 2018a, *MNRAS*, 473, 4077
 Pillepich A., et al., 2018b, *MNRAS*, 475, 648
 Planck Collaboration et al., 2016, *A&A*, 594, A13
 Prunier M., Hlavacek-Larrondo J., Pillepich A., Lehle K., Nelson D., 2024, *arXiv e-prints*, p. [arXiv:2410.21366](https://arxiv.org/abs/2410.21366)
 Rohr E., Pillepich A., Nelson D., Ayromlou M., Péroux C., Zinger E., 2024, *MNRAS*,
 Smith R. K., Brickhouse N. S., Liedahl D. A., Raymond J. C., 2001, *ApJ*, 556, L91
 Springel V., 2010, *MNRAS*, 401, 791
 Springel V., et al., 2018, *MNRAS*, 475, 676
 Truong N., Pillepich A., Nelson D., Zhuravleva I., Lee W., Ayromlou M., Lehle K., 2024, *A&A*, 686, A200
 Veronesi I., et al., 2024, *arXiv e-prints*, p. [arXiv:2411.00092](https://arxiv.org/abs/2411.00092)
 Vogelsberger M., et al., 2018, *MNRAS*, 474, 2073
 Walker S., et al., 2019, *Space Sci. Rev.*, 215, 7
 Weinberger R., et al., 2017, *MNRAS*, 465, 3291
 Zhang C., et al., 2024, *MNRAS*, 530, 4234
 Zhuravleva I., Churazov E., Kravtsov A., Lau E. T., Nagai D., Sunyaev R., 2013, *MNRAS*, 428, 3274
 ZuHone J. A., Biffi V., Hallman E. J., Randall S. W., Foster A. R., Schmid C., 2014, *arXiv e-prints*, p. [arXiv:1407.1783](https://arxiv.org/abs/1407.1783)
 ZuHone J. A., Vikhlinin A., Tremblay G. R., Randall S. W., Andrade-Santos F., Bourdin H., 2023,
 Štofanová L., Simionescu A., Kaastra J. S., 2024, The clus model in SPECT: projection and resonant scattering effects on the iron abundance and temperature profiles of galaxy clusters ([arXiv:2412.13252](https://arxiv.org/abs/2412.13252)), <https://arxiv.org/abs/2412.13252>

APPENDIX A: SPECTRAL EMISSION MODEL SYSTEMATIC UNCERTAINTIES

This section reports in detail the systematic uncertainties, associated with the choice of spectral emission model, on the inference of the true properties of the ICM, as predicted by TNG-Cluster.

Inferred - True value	bvapec	double bvapec	bvlognorm	bvgadem
Effective Temperature (kT) [keV]				
Mass-weighted central gas (all)	-1.05 (-0.75,+0.74)	-1.26 (-0.89,+1.17)	-1.21 (-0.73,+0.72)	-1.22 (-0.74,+0.77)
Mass-weighted central gas (accepted only)	-1.05 (-0.75,+0.74)	-0.64 (-0.89,+0.83)	-1.14 (-0.75,+0.63)	-1.06 (-0.66,+0.63)
Emission-weighted FoV gas (all)	0.09 (-0.24,+0.16)	-0.12 (-0.52,+0.81)	-0.08 (-0.21,+0.23)	-0.09 (-0.17,+0.24)
Emission-weighted FoV (accepted only)	0.09 (-0.24,+0.16)	0.23 (-0.89,+0.70)	-0.14 (-0.18,+0.13)	-0.06 (-0.16,+0.14)
Thermal Width Residuals ($\sigma_{kT, \text{res}}$) (2)				
Mass-weighted central gas (all)			0.40 (-0.67,+1.80)	0.92 (-1.04,+1.50)
Mass-weighted central gas (accepted only)			0.63 (-1.18,+2.23)	1.51 (-1.92,+1.74)
Emission-weighted FoV gas (all)			-1.39 (-0.01,+2.41)	0.84 (-1.01,+1.24)
Emission-weighted FoV gas (accepted only)			-2.12 (-0.01,+3.59)	1.46 (-1.55,+1.62)
Fe abundance [Solar]				
Mass-weighted central gas (all)	-0.13 (-0.11,+0.10)	-0.12 (-0.11,+0.09)	-0.18 (-0.11,+0.09)	-0.12 (-0.11,+0.10)
Mass-weighted central gas (accepted only)	-0.13(-0.11,+0.10)	-0.08 (-0.05,+0.07)	-0.15 (-0.05,+0.07)	-0.08 (-0.04,+0.06)
Emission-weighted FoV gas (all)	-0.02 (-0.02,+0.03)	-0.01 (-0.02,+0.03)	-0.06 (-0.02,+0.03)	-0.01 (-0.02,+0.03)
Emission-weighted FoV gas (accepted only)	-0.02 (-0.02,+0.03)	-0.00 (-0.02,+0.03)	-0.06 (-0.02,+0.03)	-0.00 (-0.02,+0.03)

Table A1. Absolute inference errors, i.e. differences between inferred and true values, from each spectral-emission model's inference. We report the mean difference between inferred and true value for the models used in this work. The 16th and 84th percentiles are reported with respect to the mean in parenthesis

Inferred / True value	bvapec	double bvapec	bvlognorm	bvgadem
Effective Temperature (kT) [keV]				
Mass-weighted central gas (all)	0.86 (-0.08,+0.06)	0.82 (-0.12,+0.16)	0.82 (-0.08,+0.07)	0.82 (-0.07,+0.09)
Mass-weighted central gas (accepted only)	0.86 (-0.08,+0.06)	0.88 (-0.20,+0.17)	0.82 (-0.09,+0.08)	0.83 (-0.08,+0.07)
Emission-weighted FoV gas (all)	1.05 (-0.07,+0.02)	0.99 (-0.13,+0.18)	0.99 (-0.05,+0.04)	0.99 (-0.03,+0.04)
Emission-weighted FoV gas (accepted only)	1.05 (-0.07,+0.02)	1.06 (-0.24,+0.17)	0.97 (-0.04,+0.03)	0.99 (-0.03,+0.03)
Fe abundance [Solar]				
Mass-weighted central gas (all)	0.75 (-0.19,+0.16)	0.78 (-0.20,+0.16)	0.64 (-0.17,+0.15)	0.77 (-0.20,+0.16)
Mass-weighted central gas (accepted only)	0.75 (-0.19,+0.16)	0.85 (-0.14,+0.12)	0.70 (-0.12,+0.10)	0.86 (-0.12,+0.10)
Emission-weighted FoV gas (all)	0.96 (-0.08,+0.08)	1.00 (-0.09,+0.08)	0.82 (-0.08,+0.07)	1.00 (-0.08,+0.09)
Emission-weighted FoV gas (accepted only)	0.96 (-0.08,+0.08)	1.02 (-0.06,-0.08)	0.85 (-0.05,+0.06)	1.03 (-0.06,+0.06)

Table A2. Relative inference errors, namely the ratio between the true and inferred value of the studied ICM properties throughout this paper. Similar to [Table A1](#) but for the ratio of inferred to true value instead.